

# Hydraulic Fracturing for Improved Nutrient Delivery in Microbially-Enhanced Coalbed-Methane (MECBM) Production

Sheng Zhi<sup>1</sup>, Derek Elsworth<sup>1</sup>, Jiehao Wang<sup>1</sup>, Quan Gan<sup>2</sup>, Shimin Liu<sup>1</sup>

<sup>1</sup>*Department of Energy and Mineral Engineering, EMS Energy Institute and G<sup>3</sup> Center, Pennsylvania State University, University Park, PA 16802, USA*

<sup>2</sup>*Department of Petroleum Geology and Geology, School of Geosciences, University of Aberdeen, Aberdeen, Scotland, UK*

## Abstract

Microbially enhanced coalbed methane (MECBM) recovery is a novel method to increase gas production by injecting nutrients, either with/without microorganisms, in depleted CBM wells. However, to be effective, methanogens require that the nutrient must be delivered efficiently by aqueous solution to a maximally large reservoir volume for microbial colonization. This study seeks to improve understanding of solute transport and microbial gas generation in naturally fractured reservoirs that are both pristine and hydraulically fractured. We complete a field-scale numerical simulation using an equivalent multi-continuum method to define the effectiveness of nutrient delivery. The complex pre-existing fracture pattern in the coalbed is represented by an overprinted discrete fracture network (DFN) to capture the natural heterogeneity and anisotropy of fracture permeability. A simplified PKN model is adopted to simulate hydraulic fracture propagation based on linear elastic fracture mechanics (LEFM). The hydraulically stimulated case is compared to the untreated control case, both without and with a network of natural fractures. Saturated cleat area, cumulative injection volume and prediction of methane yields are systematically modeled and analyzed for all three cases. We show that hydraulically stimulated fracture pathways, especially when connecting with a natural fracture network, optimally deliver nutrient remotely from the injection well, thereby increasing nutrient delivery and improving

methane production and potential recovery. However, large magnitudes of proppant embedment and related permeability loss in the hydraulic fractures may reduce MECBM recovery. In the optimal production scenario, the methane production rate may reach 31 ft<sup>3</sup>/ton, an approximately 5-fold increase over that from the pristine unstimulated case.

## **1. Introduction**

Coalbed methane (CBM), defined as gas vented from gassy coal seams, contributes to a widespread unconventional natural gas resource. A rapid expansion of CBM development has occurred over the past two-decades in the United States, primarily in the San Juan, Powder River, Illinois, and Black Warrior basins (Ritter et al., 2015). It has been suggested that origin of CBM is either geological (i.e. thermogenic) at low temperatures or biological (i.e. methanogenic) at higher temperatures (Park & Liang, 2016; Stolper et al., 2014). Recent field- and laboratory-scale observations have identified that active and ongoing methanogenesis pervades some sedimentary basins (Cokar et al., 2013; Kirk et al., 2012; Ulrich and Bower, 2008). If CBM can be microbially stimulated, the productive lifespans of depleted CBM wells can be extended, including generating microbial methane from areas without a prior history of gas production. Moreover, the microbially enhanced coalbed methane is an alternative method of utilizing existing coal resources, which entail restrictions on recovery due to the release of greenhouse gas and toxic emissions, i.e. sulfoxides and nitroxides, from conventional combustion of coal.

Understanding and improving the microbial process of bio-gasification is the key to enhance biogenic methane production from coal *in situ*. The biological process of microbial methanogenesis in coal has been hypothesized to begin with the solution of organic intermediates from the coal geopolymer. These soluble organics are then be biodegraded by microorganisms into substrates that are utilized by the anaerobic methanogens to produce CH<sub>4</sub>

and CO<sub>2</sub> (Jones et al., 2010). Studies have stimulated this natural bioconversion process by introducing manufactured nutrient solutions, consisting mostly of metal ions, yeast extract, peptone and methanol. Such bioconversion experiments at laboratory scale have shown that under optimal conditions, the biogenetic methane yield and content after 55 days are potentially 2900  $ft^3/ton$  and 70% from powdered Illinois bituminous coal (Zhang et al., 2016a; Zhang et al., 2015). The maximum yield from treated powdered coal from the San Juan Basin reaches 1041  $ft^3/ton$  after 30 days using a formation water-based recipe (Bi et al., 2017). Although the coal granules provide a many-fold larger surface area for microbes to colonize than the unaltered coal matrix *in situ*, the promising productivity from bio-gasification suggests the significant potential of MECBM.

Field-scale tests have also been completed in commercial wells in the Powder River and Uinta Basins to generate additional bio-gas in areas where microbial CBM production has already been present. Currently, the proposed MECBM technique is to inject nutrient, either with or without methanobacterials, into coal seams to reactivate and accelerate the growth of coal-dependent methanogenesis and to increase bioavailability of coal organics. However, methanogenesis is presumed to mostly occur inside permeable fractures and macro-pores. The meso-/micro-pores in the coal matrix are typically too small for microorganisms (Scott, 1999; Zou et al., 2013). Meanwhile, the reservoir permeability of many coal fields, such as in Illinois, is <1 mD. Extensive research has indicated that permeability is the most important factor in CBM production (Moore, 2012; Palmer, 2010; Wang et al., 2012, 2013; Wu et al., 2011). Delivery of the essential amendments into deep coal seams is limited if the reservoir permeability is too low. With insufficient nutrients present for methanogens to utilize, MECBM wells will not be economically viable. Hence, MECBM strategies for success are mainly focused on: 1)

Development of effective nutrient recipes; 2) Increasing microbial access to coal and amendments; and 3) Promotion of nutrient injection. The overarching goal of this study is focused on physically increasing fracture area for microbial colonization and the subsequent injection of nutrients.

Hydraulic fracturing is an effective method to access reservoirs, especially tight reservoirs, and to then improve oil/gas production. Based on the utility of hydraulic fracturing in conventional reservoirs, hydraulic fracturing is expected to be one potentially effective method to stimulate MECBM reservoirs. The newly generated fractures will not only provide sufficient surface area for microbial colonization, but also enhance the permeability of the coal seam for nutrient delivery. Many classic fracture models have been proposed, including PKN, KGD and penny-shaped crack models, to investigate fracture propagation during fluid injection (Nordgren, 1972; Geertsma and Klerk, 1969; Green and Sneddon, 1950). However, different from shale, coal is typically a more permeable medium with a potentially well-developed natural fracture network. With the existence of natural fractures, propagation of hydraulic fractures is commonly influenced by the in-situ stress state, material properties, viscosity and injection rate of the fracturing fluid, fracture geometry, and reservoir permeability (Huang et al., 2017; Liu et al., 2014; Rutqvist & Stephansson, 2003; Sammis & Ashby, 1986). Recently, methods coupling porosity and permeability evolution with discrete fracture network (DFN) models to represent natural heterogeneity and anisotropy have been popular, using either equivalent continuum (Gan & Elsworth, 2016; Taron & Elsworth, 2010; Oda, 1986; Rutqvist et al., 2013) or discontinuum approaches (Ghassemi & Zhang, 2006; Min & Jing, 2003; McClure and Horne, 2013; Fu et al., 2012) . Currently the investigation of hydraulic fractures in opening, propagating and in interacting with geologic discontinuities, such as natural fractures, joints, faults and bedding

planes, in a naturally fractured reservoir remains a challenge. Provided that coal has a lower strength than shale, proppant embedment in coal may play an important role in diminishing fracture conductivity. Proppant embedment, residual aperture and residual conductivity are all influenced by closure pressure, proppant size and concentration, fracture roughness, reservoir temperature, rock mineralogy and sorption behavior (Alramahi & Sundberg, 2012; Kumar et al., 2015; Lacy et al., 1998; Lee et al., 2010; Stephen & David, 2004; Zhang et al., 2013). Based on these observations, empirical expressions (Lacy et al., 1998; Volk et al., 1981; Wen et al., 2007) and analytical models (Guo et al., 2017; Jamari & Schipper, 2006; Kumar et al., 2015; Li et al., 2015) have been developed to characterize the response of propped fractures.

Descriptions of solute transport, including advection, diffusion, dispersion, sorption and chemical reaction, have been widely applied to understand the transport of solutes in reservoirs (Li et al., 2014; Liu et al., 2008; McGuire et al., 2013; Noiriél et al., 2010). In fractured rocks, the coupling of mechanical-hydrologic processes, including stress-induced changes in fracture apertures and poroelastic effects, exert a significant influence on transport properties. The compressive stress, for instance, can close fracture apertures and attenuate the dispersivity of solute components (Zhao et al., 2010). Dilated fractures will provide permeable flow pathways that result in high fluid velocities and accelerate mass transport. Effective stimulation in MECBM requires a broad sweep of the nutrient solution into the coal fracture-matrix system. This study explores such effects on solute transport in reservoirs with complex fracture geometries.

## **2. Mathematical formulation**

Reservoir and hydraulic fracture-propagation modelling are completed through the implementation of a discrete fracture network (DFN) model to accommodate solute transport inside fractures and matrix as a process-coupled multi-continuum. We implement these models in TFRact (Taron & Elsworth, 2010; Taron et al., 2009a), a TOUGH-FLAC coupling simulator, to investigate nutrient transport with fracture-matrix interactions.

### **2.1. Fractured reservoir modeling**

Coal is reasonably treated as an homogenous, isotropic and elastic continuum in many computational models (Liu et al., 2011; Rutqvist & Stephansson, 2003; Wang et al., 2013; Wu et al., 2011). The basic mechanical and hydraulic characteristics of fractures in coal may be interlinked through the theory of poroelasticity, viewed either as a single porosity or dual porosity medium (Biot, 1941; Elsworth & Bai, 1992; Zhi & Elsworth, 2016) . However, the presence of pre-existing fractures requires coal to be represented as an elastic continuum intersected by a large natural fracture network, in which fractures are assumed as twin parallel fracture walls, connected by springs in both shear and normal deformation. Fig. 1 shows how a DFN in two orthogonal orientations may be represented using the finite difference method.

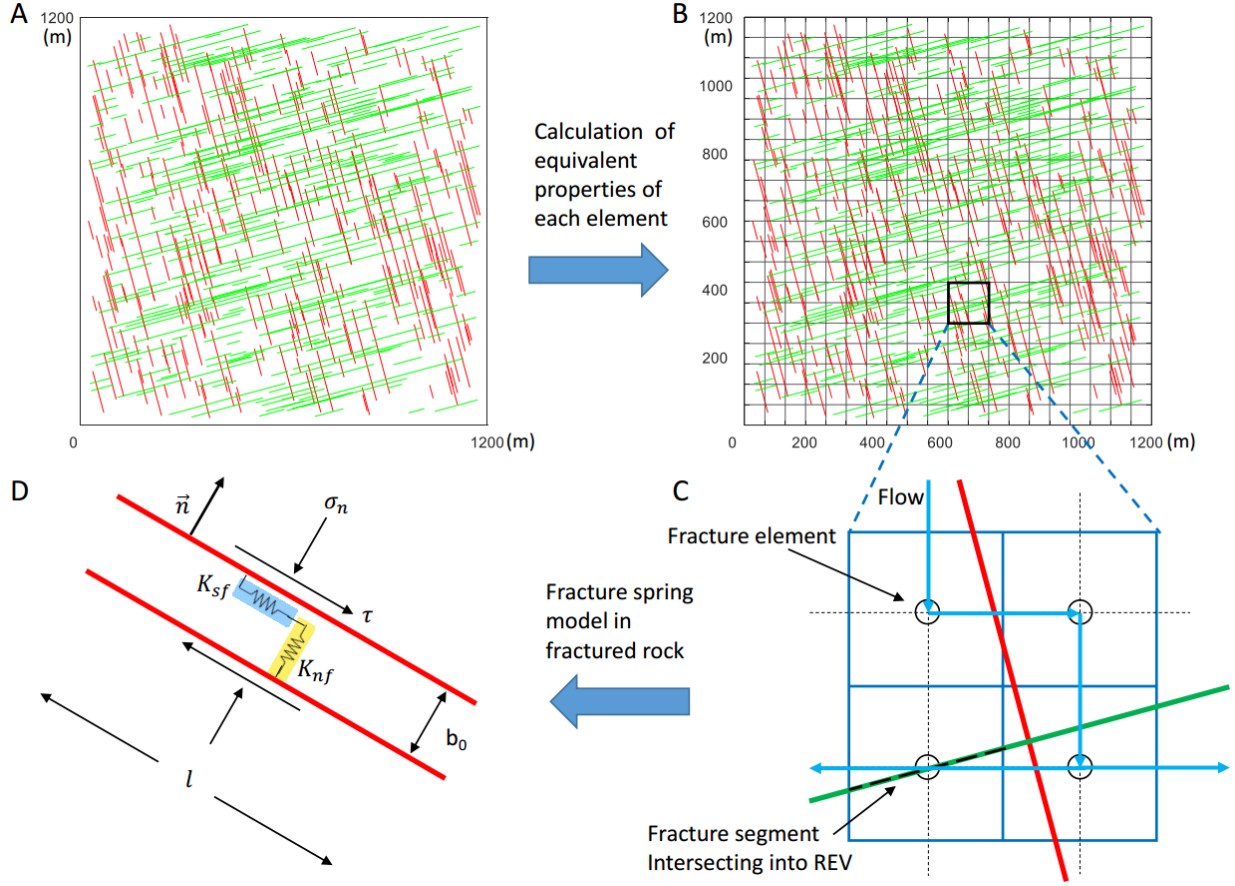


**Figure 1.** Scheme of the equivalent continuum method used in this study. (A) The original coalbed methane reservoir with DFN of two main orthogonal angles. (B) Mesh discretization used in finite difference method. (C) Schematic of how element properties influence fluid flow in the model. Red and green solid lines represent the discrete fractures. Light Blue solid lines represent the routines of fluid transport. (D) The fracture spring model.

Discrete fracture networks (DFN) of natural fractures may be used to represent the major flow channels in realistic reservoirs. The complex fracture pattern yields the heterogeneity in the fracture permeability via the topology of the flow network. It is found that the distribution of DFN follows a power-law distribution, expressed in (Fang et al., 2015)

$$p(l) = \frac{\alpha - 1}{l_{min}} \left( \frac{l}{l_{min}} \right)^{-\alpha} \quad (1)$$

where  $p(l)$  is the probability of fracture having a length  $l$ .  $l_{min}$  is the minimum fracture length.  $(\alpha - 1)/l_{min}$  is the normalizing constant.

The discrete fractures model is coupled with a continuum model to represent the fractured mass. Based on the crack tensor theory proposed by Oda (1986), the equivalent bulk modulus  $K$  and shear modulus  $G$  in each multi-continuum element can be obtained as (Gan & Elsworth, 2016; Rutqvist et al., 2013)

$$\begin{aligned} K_{eq} &= \frac{1}{\frac{1}{K_{intact}} + \sum_0^{fracnum} \frac{V_{ratio}}{b} \left[ \left( \frac{1}{K_{nf}} - \frac{1}{K_{sf}} \right) (1 - n_2^4) + \frac{1}{K_{sf}} n_1^2 \right]} \\ G_{eq} &= \frac{1}{\frac{1}{G_{intact}} + \sum_0^{fracnum} \frac{2V_{ratio}}{b} \left[ \left( \frac{1}{K_{nf}} - \frac{1}{K_{sf}} \right) (n_1^4 - n_1^2 n_2^2) + \frac{1}{K_{sf}} n_1^2 \right]} \end{aligned} \quad (2)$$

where  $K_{nf}$  and  $K_{sf}$  are fracture normal stiffness and fracture shear stiffness, respectively. Vector  $\mathbf{n}$  is the unit vector normal to each fracture.

In addition to the DFN models, the effect of poroelasticity is also integrated into the multi-continuum element. The relatively small-scale fracture system is considered homogeneously and isotopically distributed rather than being discretized as a DFN. Hence, the “matrix” in this modeling refers to a combination of both coal matrix and small partial fractures. The stress-strain relationship together with the consideration of fluid pore pressure  $p$  is

$$\varepsilon_{ij} = \frac{1}{2G} \sigma_{ij} - \left( \frac{1}{6G} - \frac{1}{9K} \right) \sigma_{kk} \delta_{ij} - \frac{\alpha}{3K} p \delta_{ij} + \frac{\varepsilon_s}{3} \delta_{ij} \quad (3)$$

where  $G$  is shear modulus,  $K$  is bulk modulus,  $\varepsilon_s$  represents sorption-induced shrinkage or swelling. Considering the Biot coefficient  $\alpha=K/K_s$ , Eq. (3) can be expressed as

$$d\varepsilon_v = -\frac{dV}{V} = \frac{1}{K} d\bar{\sigma} - \left( \frac{1}{K} - \frac{1}{K_s} \right) dp + \varepsilon_s = \frac{1}{K} (d\bar{\sigma} - \alpha dp) + \varepsilon_s \quad (4)$$

where  $\varepsilon_v$  is the volumetric strain,  $\bar{\sigma}$  is the hydrostatic stress.

## 2.2. Fracture opening model

Normal closure results from far-field stress and fluid pressure within the fracture. The reverse process to normal closure is hydraulic dilation during injection phase, as shown in Fig. 2. Based on the simplified Barton-Bandis hyperbolic-closure model, the aperture change can be formulated as (Baghbanan and Jing 2007; Gan and Elsworth, 2016)

$$b = b_0 - \frac{9b_0\sigma'_n}{\sigma_{nc} + 10\sigma'_n} + \frac{\tau - \tau_{fric}}{K_{fs}} \tan\phi_d + \frac{p_f - \sigma_n}{10 \times \frac{7\pi G}{24r}} \quad (5)$$

where  $\sigma_{nc}$ , the critical normal stress, is assumed as  $\sigma_{nc}(MPa) = 0.487b_0(\mu m) + 2.51$ .  $\sigma'_n$  is the effective normal stress and  $b_0$  is the initial aperture.  $\tau_{fric}$  is the shear friction defined by  $\tau_{fric} = S + \mu(\sigma_n - p_f)$ ,  $S$  is shear strength of the fracture,  $\mu$  is friction coefficient,  $K_{fs}$  is fracture shear stiffness and  $\phi_d$  is dilation angle.  $G$  is the shear modulus of intact rock and  $r$  is the fracture half length.

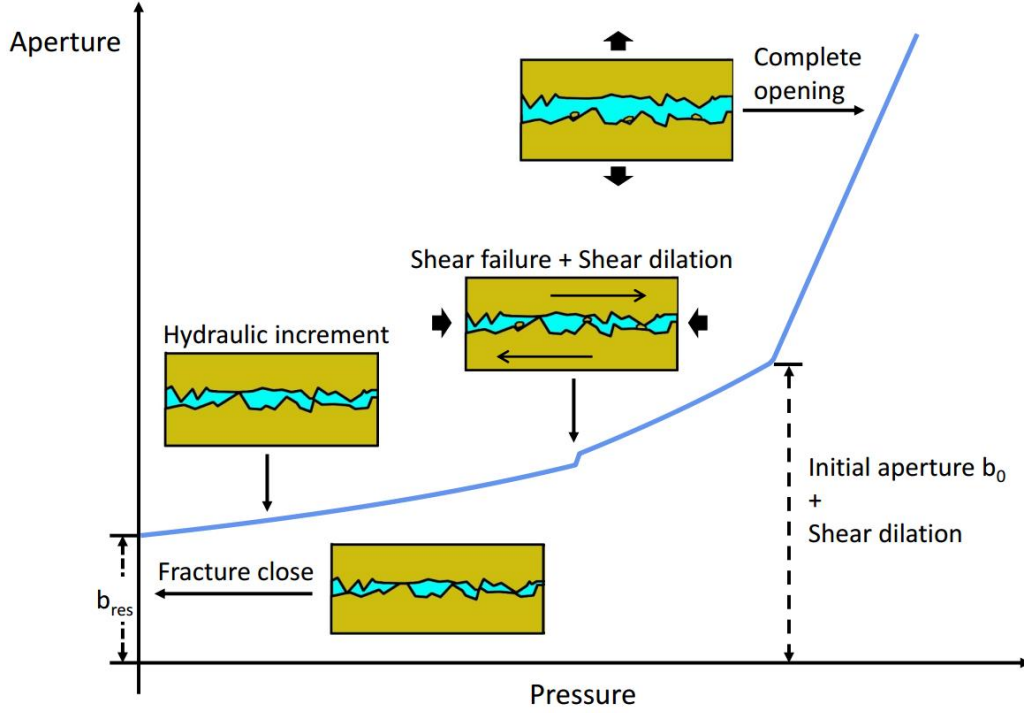


**Figure 2.** Schematic of the pressure-aperture model.

In this modeling, the volumetric strain is employed to independently calculate the porosity of the matrix and fracture. Two different equations update the porosity of fracture and matrix (Chin et al. 2000):

$$\phi_{t+1}^m = 1 - (1 - \phi_t^m) e^{-\Delta \varepsilon_v^m} \quad (6)$$

where  $\varepsilon_v^m$  is the volumetric strain of the matrix with matrix porosity  $\phi_t^m$  at time step t, and

$$\phi_{t+1}^f = 1 - (1 - \phi_t^f) e^{-\Delta \varepsilon_v^f} \quad (7)$$

where  $\phi_t^f$  is fracture porosity at time step t.  $\Delta \varepsilon_v^f$  is the change in the fracture volumetric strain, defined as  $\Delta b / b_0$ .

For a homogenous and isotropic continuum, the cubic law is typically adopted as the porosity-permeability relation for both matrix and fracture permeability evolution. The change of matrix permeability can be formulated as

$$\frac{k_m}{k_{m0}} = \left( 1 + \frac{\Delta\phi_m}{\phi_{m0}} \right)^3 \quad (8)$$

A similar equation applies in evaluating the change in fracture permeability. The permeability of discrete fractures can be calculated by the explicit fracture volume inside each mesh block. For an element containing a DFN, fracture permeability can be expressed as a sum of the permeability of the minor fractures in the matrix domain and the directional discrete fracture permeability. Hence, the integrated fracture permeability can be calculated as

$$k_{ij} = \left( 1 + \frac{\Delta\phi_f}{\phi_{f0}} \right)^3 k_{f0} + \sum^{frac_{num}} \frac{1}{12} \left( \frac{V_{ratio}}{b_0} b^3 n_k^2 \delta_{ij} - \frac{V_{ratio}}{b_0} b^3 n_i n_j \right) \quad (9)$$

where  $k_{ij}$  is the calculated tensor of fracture permeability,  $V_{ratio}$  is the fraction of the discrete fracture volume in the element volume,  $n$  is the unit normal to each fracture,  $frac_{num}$  is the total number of the truncated fractures in each element and  $\delta_{ij}$  is the Kronecker delta.

Proppant is usually pumped into opened hydraulic fractures after a certain period of water injection to maintain a reasonable fracture conductivity for the subsequent production stage. The choice of aperture opening model in the hydraulic fracture is different from that in the natural fracture. Fig. 3 shows the residual aperture due to proppant subjected to an applied normal stress in a hydraulic fracture. Residual aperture of the proppant-supported fracture is often regarded as a function of the embedment and deformation of proppants. To evaluate the residual fracture aperture, some simplifications are adopted. These include the assumption of an homogeneous

fracture surface, uniform proppant particle size, and negligible crushing and comminution of the proppant. The radius of the contact when a hard sphere is pressed against a flat surface can be expressed as (Bower et al., 1993)

$$r = R\sqrt{\frac{\sigma'}{\pi C}} \quad (10)$$

where  $R$  is radius of the proppant grain,  $\sigma'$  is effective stress applied on the flat surface, and  $C$  is cohesive strength of the surface material.

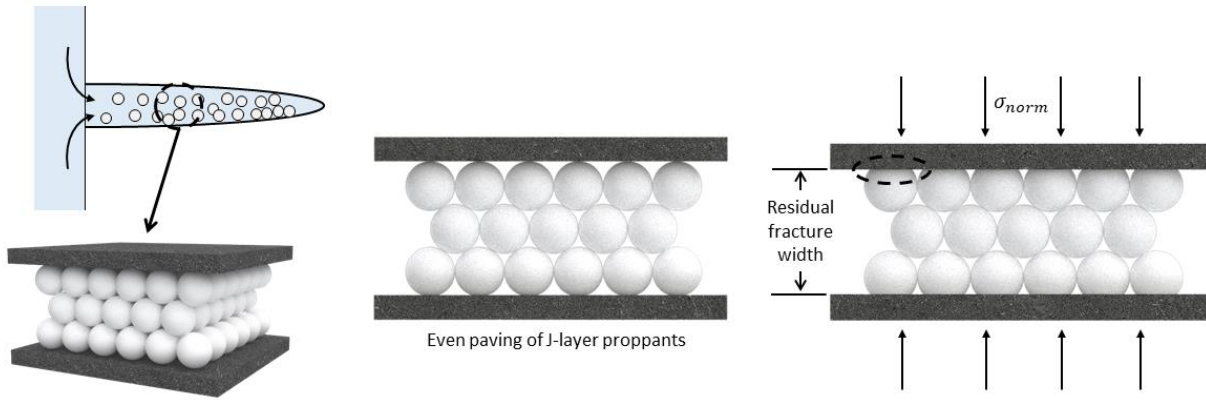


**Figure 3.** Schematic of proppant embedment and residual fracture width within an hydraulic fracture.

Embedment height  $h$  can be calculated as (Kumar & Elsworth 2015)

$$h = R\left(1 - \sqrt{1 - \frac{\sigma'}{\pi C}}\right) + \Delta D_1 \quad (11)$$

where  $R$  is radius of the proppant grain,  $\sigma'$  is effective stress applied on the flat surface, and  $C$  is cohesive strength of the surface material. Deformation of the coalbed  $\Delta D_1$  in this model is estimated as (Guo et al., 2017; J. Liu et al., 2011):

$$\Delta D_1 = \frac{\sigma'}{2E^*}(1 - R_m)D_2 \quad (12)$$

where  $E^* = \frac{1-\nu_1^2}{E_1} + \frac{1-\nu_2^2}{E_2}$ .  $\nu_1$  and  $\nu_2$  are the Poisson ratio of coalbed and proppant, respectively.

$E_1$  and  $E_2$  are elastic modulus of coalbed and proppant, respectively.  $R_m$  is the elastic modulus reduction ratio and  $D_2$  is the height of the proppant pack.

Considering proppant deformation  $\Delta D_2 = \frac{\sigma'}{E_2}D_2$ , the propped aperture of hydraulic fracture can

be calculated as

$$b = b_0 - 2R \left( 1 - \sqrt{1 - \frac{\sigma'}{\pi C}} \right) - \left( \frac{\sigma'}{E^*}(1 - R_m) + \frac{\sigma'}{E_2} \right) D_2 \quad (13)$$

where  $b_0$  is the initial aperture, here equal to  $D_2$ . For a multi-layer propped fracture, aperture change can be approximated by superposition of the deformation of each proppant layer plus the embedment from the mono-layer, since only the top-layer and bottom-layer proppants directly contact coalbed and can be embedded (Li et al., 2015).

### 2.3. DFN application

A DFN of natural fractures (NF) and hydraulic fractures (HF) may be used to represent the major flow channels in a realistic reservoir. When a hydraulic fracture intersects a discrete natural fracture during its propagation, the fracturing fluid will invade into the connected natural fracture or fracture networks. It is assumed that the fluid pressure will quickly build up inside the natural fracture due to its high permeability. The nearest fracture branch tips will continue propagating as long as the propagation criterion is met. Fluid leak-off from all the connected natural fractures

are calculated. Once the injection is completed, an evenly-paved proppant distribution is assumed inside the hydraulic fracture and the connected natural fractures of limited length.

The HF-NF geometry in the propagation processes is generated using the PKN model with a simplified fracture propagation criterion (Erdogan & Sih, 1963; Zhang & Jeffrey, 2014). Each fracture wing is generated accommodating mass conservation via a finite difference method. The fracture propagation criterion is based on the theory of linear elastic fracture mechanics (LEFM). A mixed stress intensity factor along the propagation direction is required to exceed the toughness at the onset of quasi-static crack growth. When the compression-shear wing cracks initiate under high fluid pressure, the mixed stress intensity factor at the wing crack tip can be simplified into a superposition of the two stress intensity factors, as shown in Eq. (14):

$$K_{IC} \geq K_I + K_{II} \quad (14)$$

where  $K_{IC}$  is fracture toughness of the material. The stress intensity factor at the crack tip can be obtained as (Liu et al., 2014):

$$K_I = \frac{2}{\sqrt{3}} \sigma_n \sqrt{\pi a} = \frac{2}{\sqrt{3}} (\sigma_n - p_f) \sqrt{\pi a}$$

$$K_{II} = \frac{2}{\sqrt{3}} (\tau - \mu_f \sigma_n) \sqrt{\pi a} \quad (15)$$

where  $\mu_f$  is friction coefficient. When fluid pressure exceeds the normal stress applied on fracture wall, the friction force is null. The critical fluid pressure when tension-shear damage occurs inside the coal mass is defined as:

$$p_{fc} = \sigma_n - (\sqrt{\frac{3}{4\pi a}} K_{IC} - \tau) / (1 - \mu_f) \quad (16)$$

where normal stress  $\sigma_n$  and shear stress  $\tau$  applied on a fracture oriented at azimuth  $\theta$  are:

$$\sigma_n = \sigma_1 \sin^2 \theta + \sigma_3 \cos^2 \theta$$

$$\tau = \frac{\sigma_1 - \sigma_3}{2} \sin 2\theta \quad (17)$$

Instead of initiating wing fractures, crossing may occur when fluid pressure overcomes the normal stress  $\sigma_n$  applied on the fracture walls plus the tensile stress required to break the rock. The crossing criterion can be stated mathematically as (Blanton, 1986):

$$P_{fc} > \sigma_n + T. \quad (18)$$

Since the principle of fracture propagation is to follow the least resistance (Daneshy, 2003; Liu et al., 2014), the smaller  $P_{fc}$  determines whether wing fracture extension or fracture crossing occurs. In addition, the deflection angle is negligible because the growing fractures tend to quickly align themselves to be parallel to the maximum principal stress.

After satisfying the propagation criterion, a fracture model following a PKN-formalism and based on FDM is used to estimate the propagation of the hydraulic fracture during ongoing injection. Fluid flow in the dilating HF portion is based on the lubrication equation

$$\frac{\partial q}{\partial x} + \frac{\partial w}{\partial t} + u = 0 \quad (19)$$

where  $w$  is width of hydraulic opening,  $q$  and  $u$  are, respectively, flow rate and leak-off term for unit fracture height.

It is assumed that the flow of the Newtonian fracturing fluid within the fracture is laminar and within a channel of elliptical cross-section. The expression for average local flux can be written as:

$$\bar{q} = -\frac{\bar{w}^3}{\pi^2 \mu} \frac{\partial p}{\partial x} \quad (20)$$

where  $\mu$  is the dynamic viscosity of the fluid. A one-dimensional fluid leak-off is considered in accordance with Carter's model (Rahman and Rahman, 2010)

$$u = \frac{C_l}{\sqrt{t-t_0(x)}} \quad (21)$$

where  $C_l$  is the leak-off coefficient.

The global mass conservation is based on the principle that the volume of the injected fluid is equal to the volume of the fracture and the cumulative leak-off volume (Detournay et al., 1990).

The generated fracture length  $L$  can be obtained by solving the global equation

$$\int_0^{L(t)} \omega(x,t) ds + \int_{t_0(x)}^t \int_0^{L(t_0)} u(x,\tau) dx dt = \int_0^t q_0(t) dt \quad (22)$$

For the wing fractures that initiate from the tips of a pre-existing fracture, the equation above can be written as

$$\int_0^{L_{n0}+L_n(t)} \omega(x,t) dx + \int_{t_{n0}(x)}^t \int_0^{L_{n0}+L_n(t)} u(x,t) dx dt = \int_{t_{n0}(x)}^t q_{n0}(t) dt \quad (23)$$

where  $n$  denotes fracture propagation index and  $t_{n0}$  is the start time of the  $n$ -th fracture branch and  $t$  is the arrival time of the  $n$ -th fracture tip at location  $x$ .  $L_{n0}$  is the total fracture length connected with the new branch.

## 2.4. Solute transport

We represent solute transport through conservation of dissolved mass in a porous medium using the flow equation to define Darcy velocity

$$\frac{\partial M_k}{\partial t} = -\nabla F_k + Q_k \quad (24)$$

where  $\Delta M = \Delta(\phi\rho)$  is fluid mass accumulation,  $F$  is mass flux from Darcy's law, and  $Q$  is mass source/sink. The subscript  $k$  is phase index for flow.

Solute transport includes advection, diffusion and dispersion. In a porous medium, the effect of diffusion is generally smaller in comparison to the dispersion process. Hence, the hydrodynamic dispersion coefficient  $D$  is typically adopted as a summation of the mechanical dispersion coefficient  $D_m$  and the effective diffusion coefficient  $D_e$ . In 2D systems, the general Advection-Dispersion Equation (ADE) is:

$$\frac{\partial M_k}{\partial t} = -\nabla \cdot (\mathbf{u}C_{jk} - D\nabla C_{jk}) + Q_k \quad (25)$$

where  $C_{jk}$  is the tracer concentration for the  $j$ -th component and  $\mathbf{u}$  is Darcy velocity.

### 3. Simulation design

A prototypical MECBM reservoir under in-situ stresses and  $1200 \text{ m} \times 1200 \text{ m} \times 10 \text{ m}$  is used in this study. Three cases are simulated to compare fluid flow and solute transport for different scenarios. Both natural and hydraulically-driven fractures are represented by a DFN coupled into the multi-continuum model. The following defines how these models are assembled.

#### 3.1 Biogeochemical Controls

Most methanogens commonly inhabiting coalbed reservoirs are members of a single phylum, the Euryarchaeota, belonging to the domain of Archaea (Lloyd, 2015). In addition to methanogens, the collective actions of fermentative and acetogenic bacteria are required for microbial bioconversion from coal to methane. First, the complex organic matter in coal is decomposed to simpler molecules, i.e., acetate, long chain fatty acids, and  $\text{HS}^-$ , by fermentative anaerobes. Fatty

acids, alcohols, and some aromatic and amino acids are then transformed to H<sub>2</sub>, CO<sub>2</sub>, and acetate by H<sub>2</sub>-producing acetogens. Eventually, those simple molecules are converted to CH<sub>4</sub> by methanogens (Faiz & Hendry, 2006). All the microbial communities involved in methanogenesis are ubiquitous and in elevated concentrations in the formation water and coal in biogenic coalbed methane reservoirs (Stolper et al., 2014; Ji Zhang et al., 2015). In this study, the presence of these necessary microbial communities promoting methanogenesis is presumed in the stimulated coalbed methane reservoir.

Coalbed methanogens, if properly nurtured, can increase methane production from existing wells. Typical nutrient recipes comprise four major ingredients: 1) mineral solutions, such as: Mg<sup>2+</sup>, Ca<sup>2+</sup>, Na<sup>+</sup> and K<sup>+</sup>; 2) vitamin solutions, such as: vitamin B12, thiotic acid and nicotinic acid; 3) trace metal elements, such as: B, Zn, Co, Mo and Fe; 4) organic matter, such as: yeast extract and peptone as nitrogen sources (Green, et al., 2008; Zhang et al., 2016b). Given the high hydraulic gradient that is present between injection and the far field within reservoir, flows are advection dominated with mechanical dispersion and diffusion mechanism of the prevailing mixing. Thus, differences between diffusion coefficients of the various solutes in the nutrient recipes are negligible and hydrodynamic dispersion dominates mixing at the solute front. Therefore, the injected nutrient is considered as a tracer and its concentration is normalized to 1.0 (the optimal condition for nutrient).

### **3.2. DFN generation of natural fractures**

Discrete fracture networks with appropriate mechanisms coupling mechanical response play a significant role in understanding how a connective fracture system channels fluid flow (Long & Witherspoon, 1985). Two sets of discrete fractures are constructed at azimuths (from the North) of 075° and 165° in a 1200 m × 1200 m × 10 m coalbed methane reservoir. Since the length of

each individual fracture is set in the range of 40 – 300 m and  $\alpha=1.5$ , the equation of this power-law distribution becomes

$$p(x) = 0.025 \left( \frac{x}{20} \right)^{-1.5} \quad (36)$$

where  $p(x)$  is the probability for a single fracture of length  $x$ . In total 200 fractures (100 fractures for each orientation of two sets) are randomly distributed in the simulated domain. A natural fracture system comprises smaller fractures representing local fractures/joints and larger fractures representing large-scale geological faults in the coal seam. In this DFN modeling, minor natural fractures with lengths  $<40$  m are incorporated into the matrix domain in the multi-continuum element using an equivalent continuum approach. Fig. 6 shows a histogram of the fracture probability distribution for one fracture set.

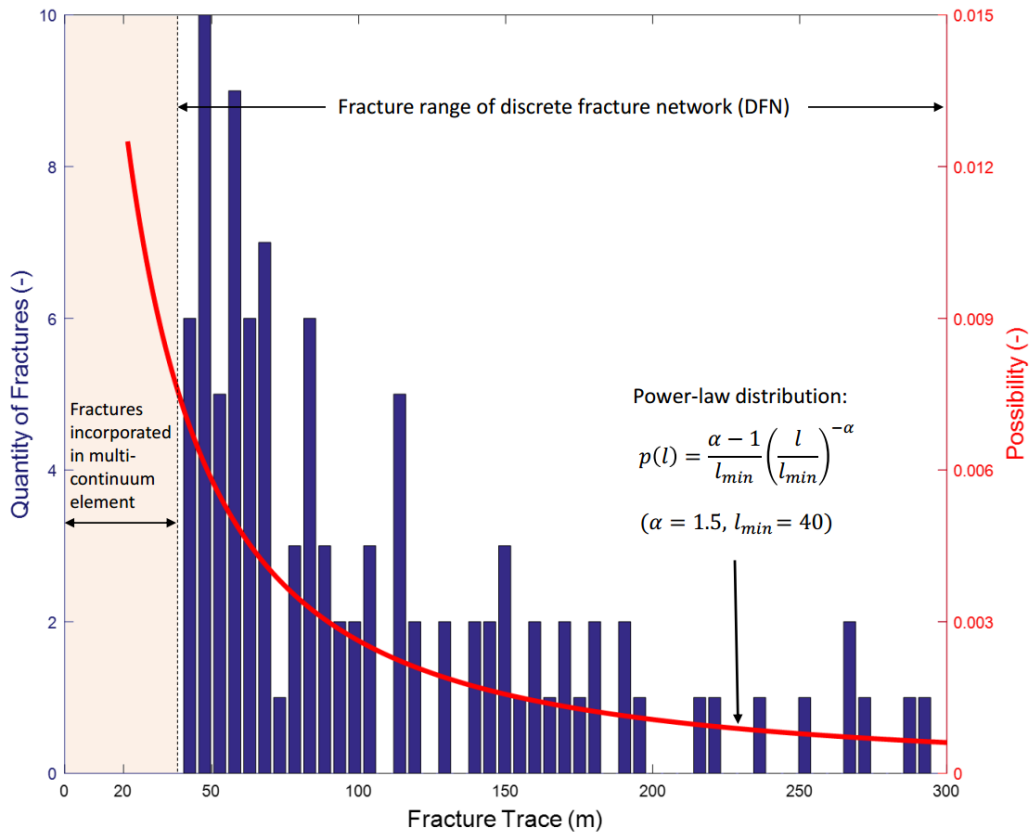


**Figure 6.** Histogram of fracture lengths and their probability distribution for an example of 100 fractures.

Initial aperture  $b_i$  for each fracture is proportional to its length  $l$ , following a power law function (Gan & Elsworth, 2016; Olson, 2003). Distribution of the initial fracture aperture is plotted in Fig. 7. Heterogeneity of the natural fracture network has been incorporated into the properties of the multi-continuum elements. Initial fracture porosity and permeability are calculated based on the properties of both the fracture and matrix. Initial fracture porosity is the ratio between the overall fracture volume within the single element and the entire element volume. Initial fracture permeability is calculated using Eq. (9) with the fracture porosity determined in the prior time/iteration step.

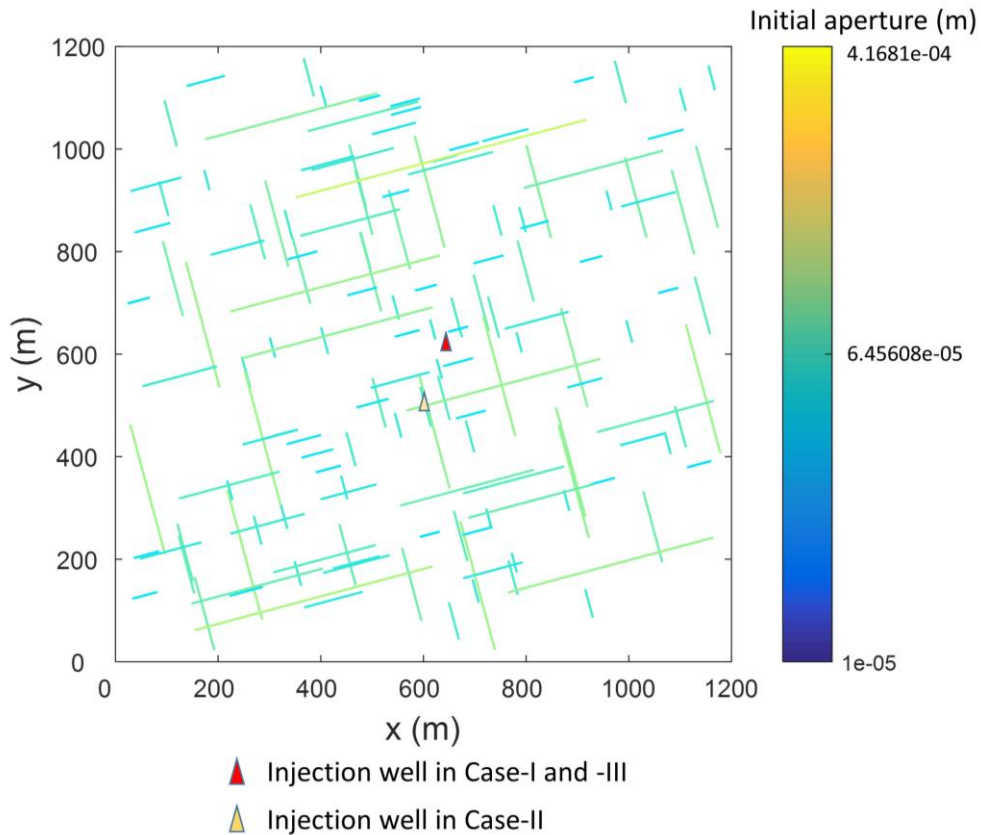


**Figure 7.** Distribution the initial apertures of the two sets of discrete fractures.

### 3.3. Characteristics of example cases

Reservoir properties in this study are listed in Table 4. The maximum and minimum principal stresses are set to 20 MPa (E-W direction) and 16 MPa (N-S direction), respectively. Before injection, an initial reservoir pressure of 1 MPa is assigned to represent depleted fluid pressure in the reservoir due to prior water and gas production. In the default scenario, injection pressure is set to 14 MPa, which is close to the closure stress applied on the hydraulic fractures.

The layout of the injection well is also shown in Fig. 7. In Case-I and -III, the injection wells are located in the same position, approximately 50 m out from the neighboring DFN. The injection well for Case-II is sufficiently close to a long fracture oriented at an azimuth of  $075^\circ$  within the fracture network. This results in the injection well being connected to the pre-existing permeable fracture networks. To summarize, the injection wells are located at (650,610) in Case-I and -III, and at (610,510) in Case-II. The first two cases are used to examine the effects of mass transport using matrix and the natural fracture network stimulated at below the minimum principal stress, respectively. Case-III is for stimulation of the naturally fractured reservoir by hydraulic fracturing. Key modeling parameters are listed in Table 4.

**Table 4.** Modeling parameters for the numerical simulation.

<b>Parameter</b>	<b>Value</b>
Young's modulus of coal ( $E$ )	2.45 GPa
Poisson's ratio of coal ( $\nu$ )	0.3
Density of coal ( $\rho_c$ )	1220 kg/m <sup>3</sup>
Fluid dynamic viscosity ( $\mu$ )	$0.653 \times 10^{-3} Pa \cdot s$
Temperature (T)	313.14 K
Injection pressure ( $P_f$ )	14 MPa
Maximum confining stress ( $\sigma_1$ )	20 MPa
Minimum confining stress ( $\sigma_3$ )	16 MPa
Initial reservoir pressure ( $P_{f0}$ )	1.0 MPa

Fracture angle ( $\theta$ )	75/-15°
Initial matrix permeability ( $k_{mo}$ )	$1.0 \times 10^{-17} \text{ m}^2$
Initial fracture permeability ( $k_{fo}$ )	$0.5 \sim 2.5 \times 10^{-16} \text{ m}^2$
Initial joint normal stiffness ( $k_n$ )	5 GPa/m
Initial joint shear stiffness ( $k_s$ )	50 GPa/m
Biot's coefficient ( $\alpha$ )	0.9
Simulation time (t)	30 day

### 3.4. Hydraulic fracture propagation

As discussed previously (Section 2.3), the mechanics of fracture initiation is based on LEFM theory using a toughness criterion. Wing fractures grow when the mixed stress intensity factor along the propagation direction is equal to the toughness at the onset of quasi-static crack initiation (Erdogan & Sih, 1963). A commonly used PKN model is adopted to shape the generated hydraulic fractures. The modeling properties used in this propagation method are shown in Table 5. The propagated length of the hydraulic fracture is calculated by solving the global equations Eq. (26) and Eq. (27) in MATLAB. In terms of interaction with natural fractures, it is assumed that the hydraulic fractures have identical leak-off behavior to the pre-existing natural fractures. The propagation of hydraulic fractures in case-III is illustrated in Fig.8. The blue solid lines represent the bi-wing hydraulic fractures and propped natural fractures. The arrays of short blue bars represent pressure profiles at specific times. The pressure profile above each hydraulic fracture is defined at the moment when it interacts with the DFN.

**Table 5.** Modeling parameters for hydraulic fracturing.

Parameter	Value
Young's modulus of coal ( $E$ )	2.45 GPa
Poisson's ratio of coal ( $\nu$ )	0.3
Fluid dynamic viscosity ( $\mu$ )	0.05 Pa·s

Injection flow rate ( $Q_0$ )	$0.03 \text{ m}^3 / \text{s}$
Coal seam thickness ( $h$ )	10 m
Leak-off coefficient ( $C_L$ )	$1 \times 10^{-6} \text{ m} \cdot \text{s}^{0.5}$
Cohesion (C)	3.0 MPa
Biot's coefficient ( $\alpha$ )	0.9
Simulation time (t)	100/500/1500/2500 s

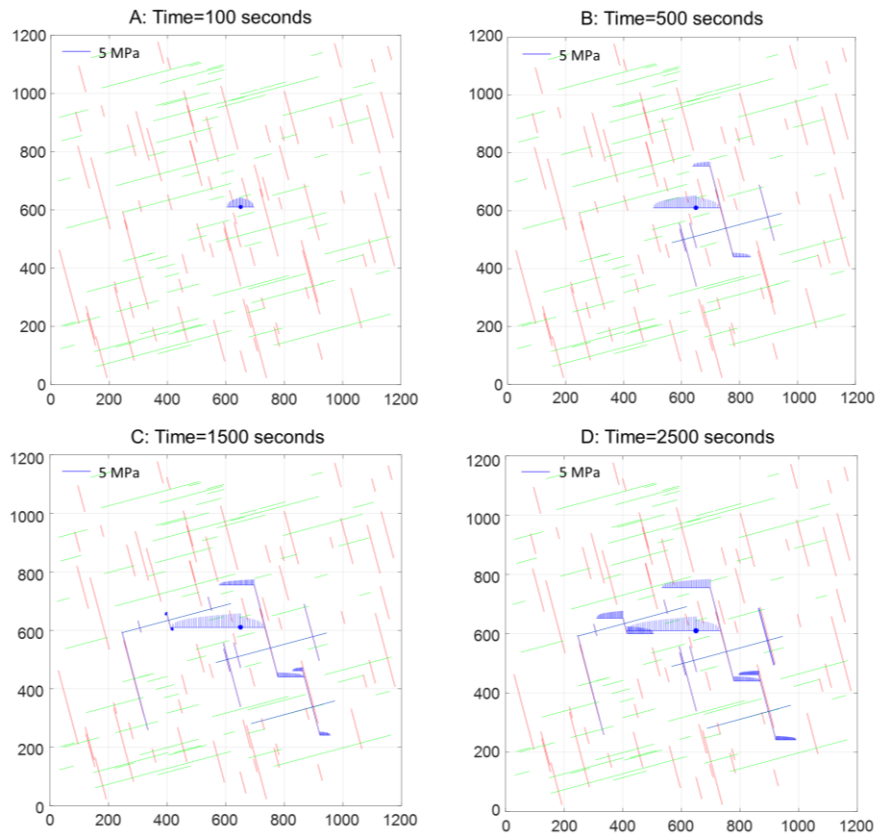


**Figure 8.** Propagation of hydraulic fractures at different times in case-III. The blue solid lines represent the bi-wing hydraulic fractures and natural fractures into which proppant has washed. The arrays of short blue bars represent pressure profiles at certain injection times. The pressure profiles are defined at the moment they interact with the DFN.

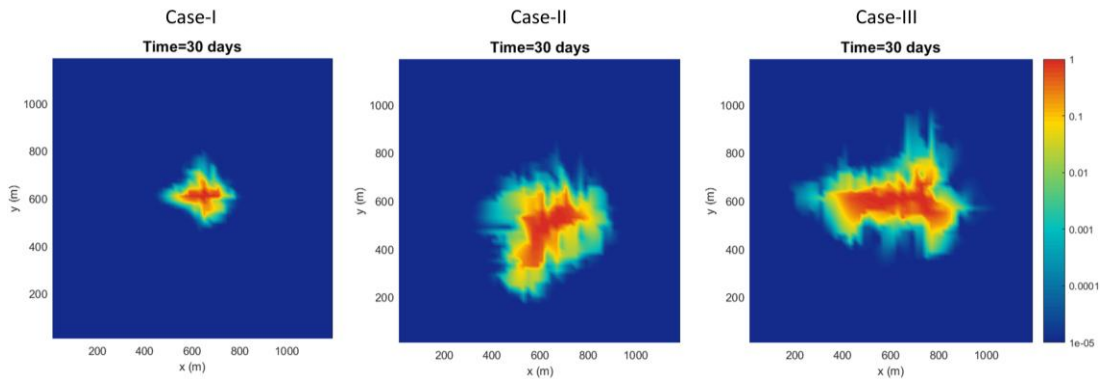
## 4. Results and discussion

Here we present a prototypical MECBM represented by a pseudo 3D model domain of  $1200 \text{ m} \times 1200 \text{ m} \times 10 \text{ m}$  at isothermal conditions of  $40^\circ\text{C}$ . As introduced above, a maximum principal stress (E-W direction) of 20 MPa and a minimum principal stress (N-S direction) of 16 MPa are applied on the lateral boundaries. A vertical stress of 24 MPa is applied on the top as the overburden. Boundary conditions are applied at time  $t=0^-$  to equilibrate with initial pore pressure of 1 MPa. The injection pressure is set constant in time at 14 MPa in all three cases.

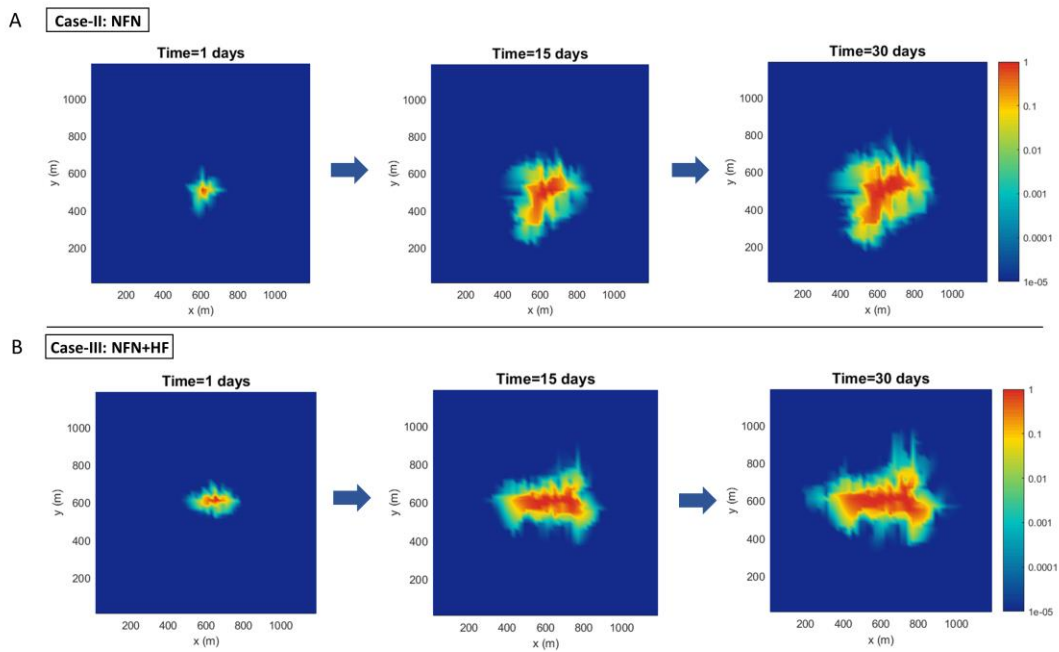
### 4.1. Concentration distribution

After injection for 30 days, the distribution of relative concentrations (RC) in the three cases are shown in Fig. 9. Note that there is no discrete fracture near the inlet in Case-I, although permeability of the small fractures ( $<40\text{m}$ ) in the non-discretized matrix have been considered as  $k = k_m + k_f$ . Hence, solute transport is only dependent on the matrix diffusion in Case-I. Clearly, the solute in Case-I is delivered the shortest distance and spreads over the smallest area among the three cases. Nutrient distributions of the other two cases demonstrate a map of penetration that is strongly shaped by DFN geometry. Cases-II and -III demonstrate that the discrete fractures play a pivotal role in solute transport. The pre-existing fracture network dramatically enhances the solute transport in Case-II when compared to Case-I. In Case-III, the penetrated area of the reservoir is dominated by the newly-generated hydraulic fractures in the E-W orientation. The resultant flow pattern is influenced by the interconnected HF-NF network, which has a larger reach than in the case of the pristine NF network in Case-II. Fig. 10 illustrates how the relative concentration evolves with the duration of injection in Cases-II and -III. The saturated area of  $\text{RC} > 0.1$  in Case-III is larger than that in Case-II, especially after the first day of injection - due to the higher permeability of the propped hydraulic fractures. Comparing 30-day

injection with the 1-day and 15-day injections, the spreading rates of the high-concentration areas in both cases reach their maximum in the early stage of injection and then the rate of growth gradually declines with continuing injection. This is because the reservoir pressure gradually equilibrates to the injection pressure and thus advective transport is replaced by diffusion.



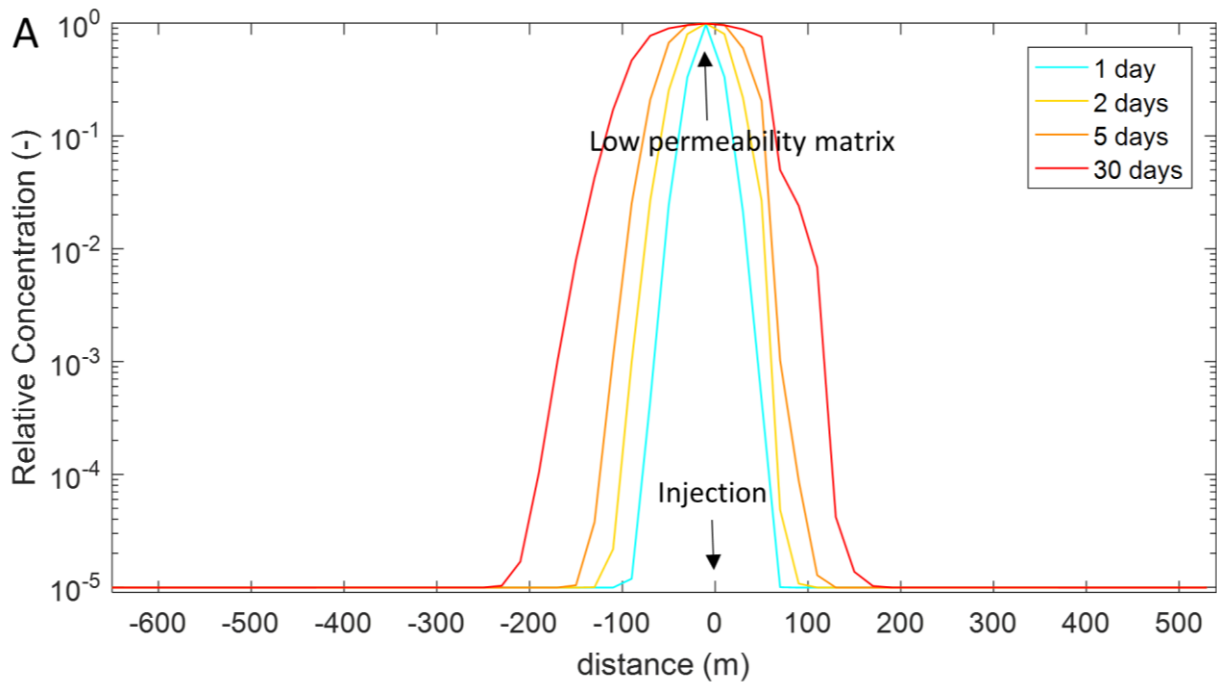
**Figure 9.** Relative concentration distributions in the reservoir after 30-days of injection for the three different cases.



**Figure 10.** Relative concentration distributions in the reservoir vs. injection time for Case-II and Case-III.

To illustrate the solute flow path during injection, a cross section through the injection well in the E-W direction is chosen to construct cross-sections of relative concentrations, shown in Fig. 11. Fig 11(A) shows an approximately symmetric distribution of mineral concentration due to the homogeneity of the matrix near the injection well in Case-I. However, asymmetric distributions of solute concentration can be seen in the other two cases because of the presence of the DFN. A steep concentration gradient evolves from the inlet to the plume front after the first day in Case-I, while the surrounding areas gradually become fully saturated after 30 days. However, only 70 m outward from the injector is permeated at  $RC > 0.8$  when the injection ends. Fig.11(B) shows solute transport via the coal matrix which is strongly influenced by the adjacent natural fracture networks. In case-II, solute first is transported through the connected natural fracture network. Then, the high-concentration solute in the fractures is carried to the nearby matrix by the hydraulic gradient between the fracture and matrix. After 30-days of injection, solute of  $RC > 0.8$  is transported to about 100 m and 50 m from the injector in the East and West directions, respectively. The natural fracture connected to the injector shows a strong influence until the flow reaches the end of the fracture in the E-W direction. Fig. 11(C) illustrates the enhancement in nutrient delivery that evolves inside the hydraulic fractures. Different from the angled nature fractures, the hydraulic fractures in Case-III have the same orientation with the maximum principal stress. After 10-days of injection, the relative concentration curve is remarkably flat near the injection well instead of replicating the steep gradients of Cases-I and -II. This reveals that along the cutting direction, the 10<sup>th</sup>-day of injection after hydraulic fracturing results in a better nutrient delivery than after 30-days of injection in Case-I. After 30-days of injection, the nutrient concentration reaches full saturation from -140 m to 130 m in the cross-cutting direction. A moderate decline occurs in the range -170 m to -420 m due to mass

transport from the propped natural fractures. A steep drop of RC occurs for propagation in the opposite direction because the HF propagation ceases at a NF oriented at an azimuth of  $165^\circ$ . The spiked-shape of the concentration profiles in Figs. 11(B) and (C) results from intersections between the section and the fracture networks. This shows that indeed the nutrient is readily and effectively transported along a tortuous fracture network.



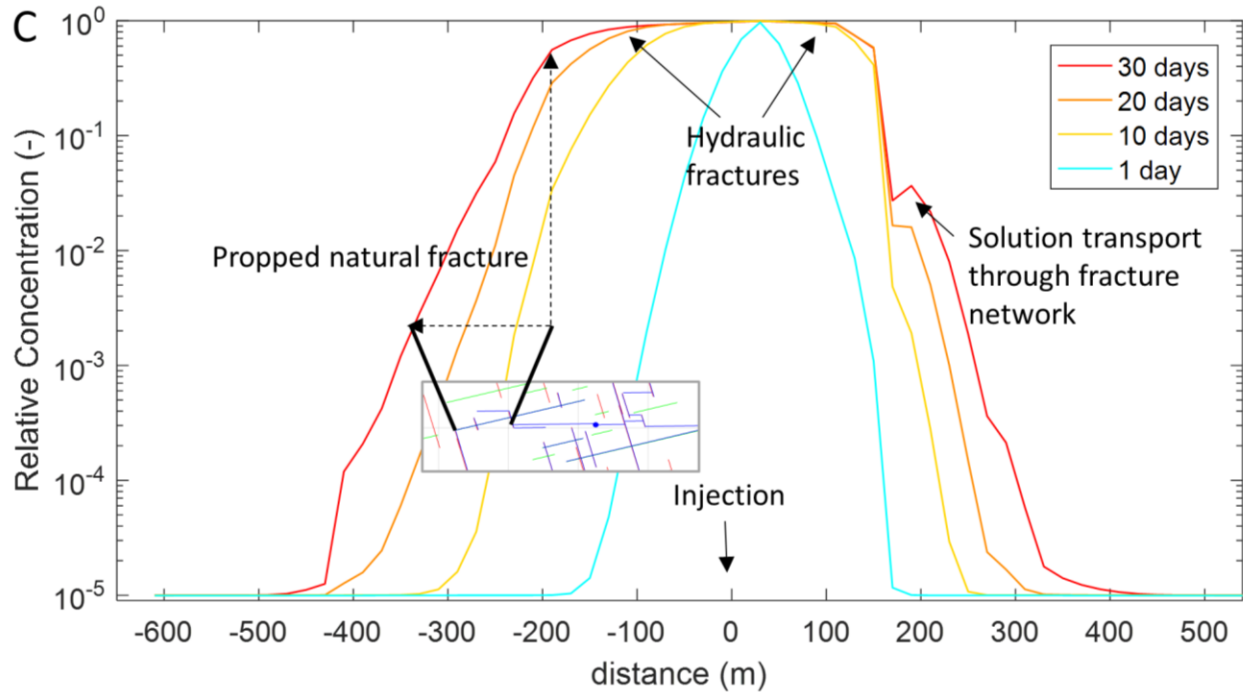
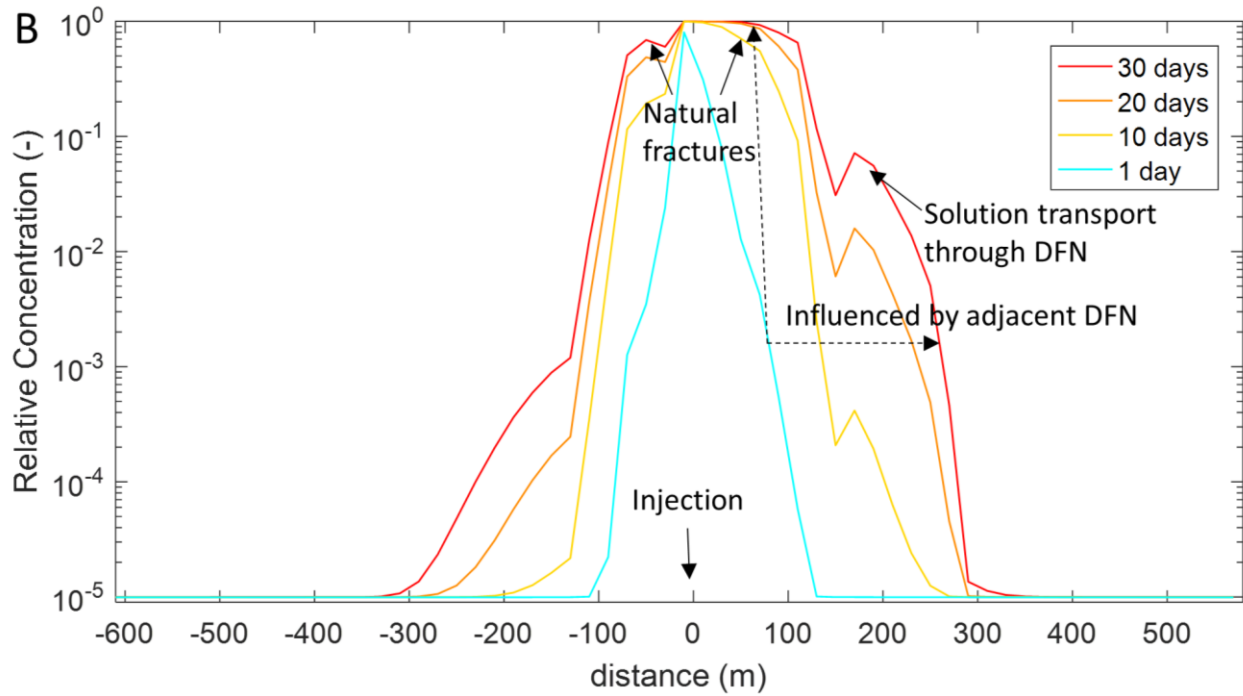


**Figure 11.** Change in relative concentrations at 1 day, 10 days, 20 days and 30 days for the three cases.

The heterogeneity of the concentration distribution (Figs. 9, 10, 11) demonstrates the influence of the three different media on solute transport - coal matrix (Case-I), the natural fracture network (Case-II) and the NF network stimulated by hydraulic fracturing (Case-III). Since there are two different fracture sets comprising the natural fractures in the simulated coal reservoir, totally four types of media are investigated, as shown in Fig. 12. Locations that are 80 m outward from the inlet are selected to monitor the evolution of concentration. The red curve at the top shows a typical pattern of concentration evolution for a newly-generated hydraulic fracture. Concentration in the hydraulic fracture increases exponentially after injection begins and then gradually reaches an equilibrium concentration ( $RC=1.0$ ). In this case, relative concentration reaches 0.8 and 0.5 only after 5.4 and 10.9 days of injection, respectively. The slowdown in the rate of growth is primarily caused by the reduced advection in the hydraulic fractures. The two blue curves represent two different patterns of concentration accumulation in pre-existing natural fractures. The upper solid blue curve shows how solute concentration builds in the natural fracture oriented at an azimuth of  $075^\circ$ , oriented only at  $15^\circ$  to the maximum principal stress. The relatively smaller normal stress promotes the creation of a permeable pathway for solute transport and results in a rapid pressure build-up distant from injection. Therefore, the relative concentration increases rapidly and then gradually slows when  $RC > 0.75$  (in this case) akin to that observed for the hydraulic fracture. The lower dashed blue line represents a distinctly different pattern of concentration growth in natural fractures that are subject to a larger normal stress. The larger restraining stress on the fracture walls induces a smaller initial fracture aperture and requires a higher opening pressure. Therefore, instead of increasing rapidly, the concentration initially grows only slowly. After fluid pressure rises and the fracture permeability increases, the rate of increase in concentration is gradually enhanced. The enhanced delivery

capacity of the hydraulic fracture can be seen when compared to the natural fracture. The slow build-up of concentration in a nearly linear trend in matrix is also shown as the grey line in Fig. 12.

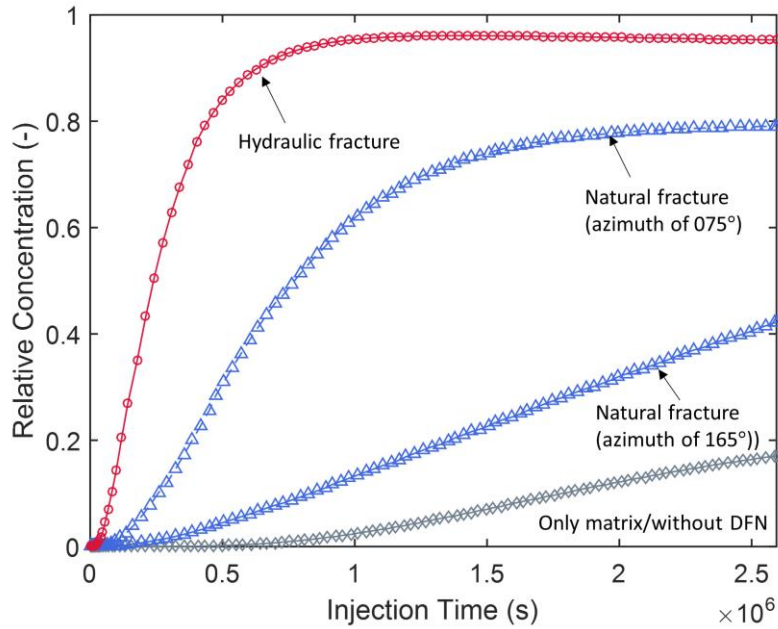


**Figure 12.** Concentration evolution for different matrix/fracture types. All the monitored locations are 60 m outward from the injection well.

#### 4.2. Nutrient abundance

In addition to the normalized tracer concentration, it is important to estimate the absolute mineral abundance that has been injected into the CBM reservoir. The evolution of cumulative injected nutrient volume is plotted using a logarithmic scale in Fig. 13 (A). The eventual injection volumes of nutrient in the three cases are  $2.8 \times 10^4$  L,  $1.23 \times 10^5$  L and  $8.9 \times 10^5$  L, respectively. The influence of the fracture channel on nutrient delivery is distinct since the total injected volumes in Case-II and Case-III are ~4 to 32-fold larger than the base case. The accumulation rate of the injection becomes linear after a short period of injection. These phenomena can also

be observed in Cases-II and -III. The evolution of injection rate at a constant injection pressure for each case is shown in Fig. 13(B). The slope of the flow rate corresponds to the trend in cumulative injection volume. Due to its larger permeability, injection rate in the hydraulic fracture network is always higher than that in pre-existing fractures under the current configuration. Compared with Case-II, a larger maximum injection rate in Case-III is reached early and results in an approximately 8-fold increment of injection volume.

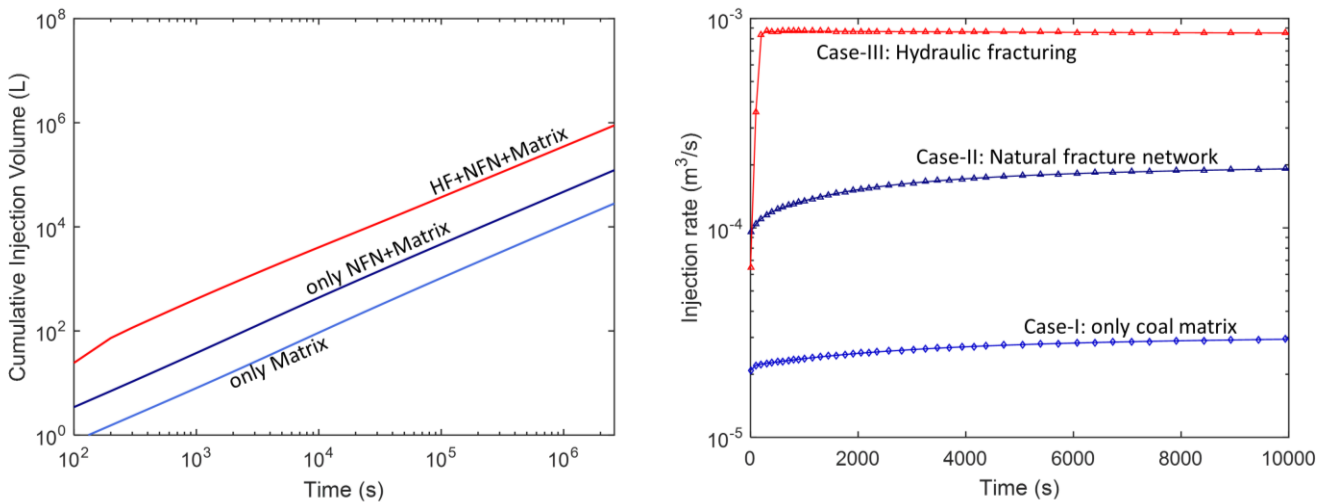


**Figure 13.** (A) Cumulative injected volume of nutrient versus injection time; (B) Injection rates in first 10000 seconds injection (Injection pressure is set to 14 MPa).

### 4.3 Saturated cleat area

Recent studies suggest that it is the coal cleat system where methanogens interact with the coal and injected nutrient (Ritter et al., 2015; Scott, 1999). The enhanced bio-gasification effect is dependent upon the area of the saturated cleat surface after nutrient injection. Although the macropore space (>1000 nm) may also partially provide microbial access to bacteria, its effect is difficult to rigorously quantify due to the diversity of microbe species and sizes. Therefore, only the surface area of the cleat system and the DFN are considered in the evaluating the effective methanogenesis in this study. Fig. 14 shows the linear relation between cleat spacing and cleat

surface area. For a cleat spacing of 10 cleat/inch (4 cleat/cm), the total cleat surface area will be  $1.94 \times 10^3 \text{ m}^2/\text{ton}$ , whereas a cleat spacing of 0.1 cleat/inch (0.4 cleat/cm) will have a cleat surface area of  $19.36 \text{ m}^2/\text{ton}$ . This estimation is on the basis of an homogenous and isotropic cleat distribution. In this study, we assume an average cleat surface area of  $600 \text{ m}^2/\text{ton}$  (2.5 cleat/inch). A concept of saturated cleat area (SCA) is introduced to investigate the saturation state of the treated reservoir. Cleat area saturated by solute is defined as a summation of the fracture surface area of the DFN and the average cleat surface area at a certain concentration. Four relative concentration tiers from  $>0.0001$  to  $>0.1$  at 10-fold intervals are used. For each multi-continuum element, SCA can be calculated by the following equation if the relative concentration in this element is larger than a certain threshold:

$$SCA = \sum_{n=1}^{frac_{num}} 2l_n h + A_0 V_e \rho \quad (37)$$

where  $frac_{num}$  is the number of discrete fractures within the element,  $V_e$  is the element volume,  $l_n$  is the length of the  $n$ -th segmented fracture,  $A_0$  is the average cleat surface area per ton of coal and  $\rho$  is coal density (here  $1220 \text{ kg/m}^3$ ).

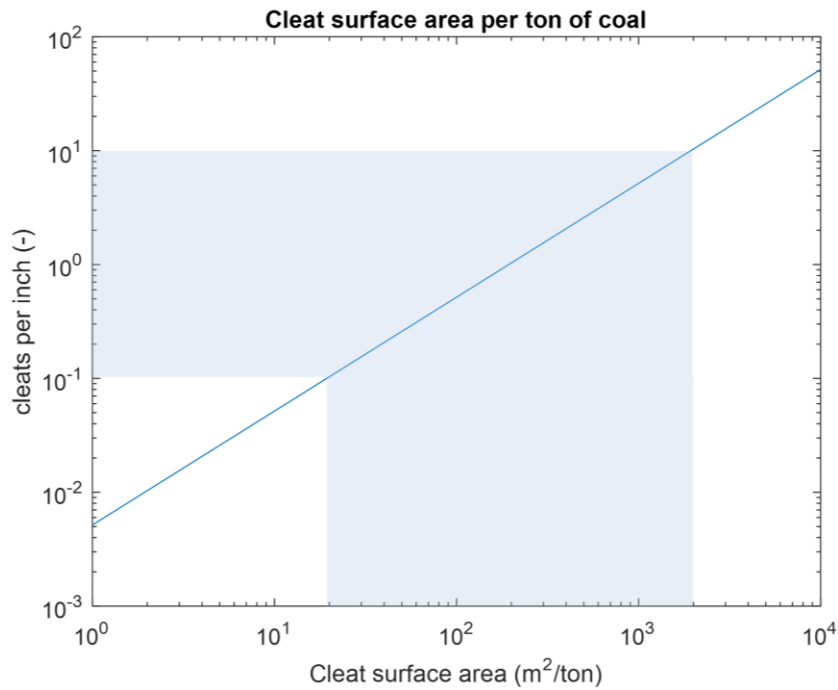


**Figure 14.** Relation between cleat spacing and cleat surface area per ton of coal based on the assumption of an homogenous and isotropic cleat distribution. Macropore space ( $>1000$  nm) may also partially provide microbial access to bacteria, but its effect is difficult to be rigorously quantified. Hence, only the cleat surface area and surface of the DFN are considered for methanogenesis in this study.

Fig. 15 shows that SCA increases with injection time in the three modeling cases. In each RC range, the SCA rises at a faster rate at the beginning and then decreases to a flat linear trend. This reveals that the solute transport gradually changes from advection to diffusion. Each concentration tier sweeps approximately the same surface area in all cases. It is worth noting that the concentration tiers are at 10-fold intervals. This indicates that simply increasing nutrient concentration at inlet may have a low efficiency in increasing the swept surface area to an optimal concentration. After 30-days of injection, the hydrofracturing case (case-III) provides a saturated surface area of  $1.19 \times 10^5 \text{ m}^2$  for  $\text{RC} > 0.1$ , while nearly half of this is only accessed ( $0.75 \times 10^5 \text{ m}^2$ ) for Case-II. Not surprisingly, Case-I has the lowest saturated area of  $1.63 \times 10^4 \text{ m}^2$

for  $RC > 0.1$ . Fig. 15 (D) also shows that SCA increases slowly at the conclusion of the injection for  $RC > 0.1$  in Case-II, whereas the retardation trend does not appear in any RC tier in Case-III. This is because the hydraulic fractures play an important role in delivering solute to the connected remote natural fracture system even at end stage of injection.

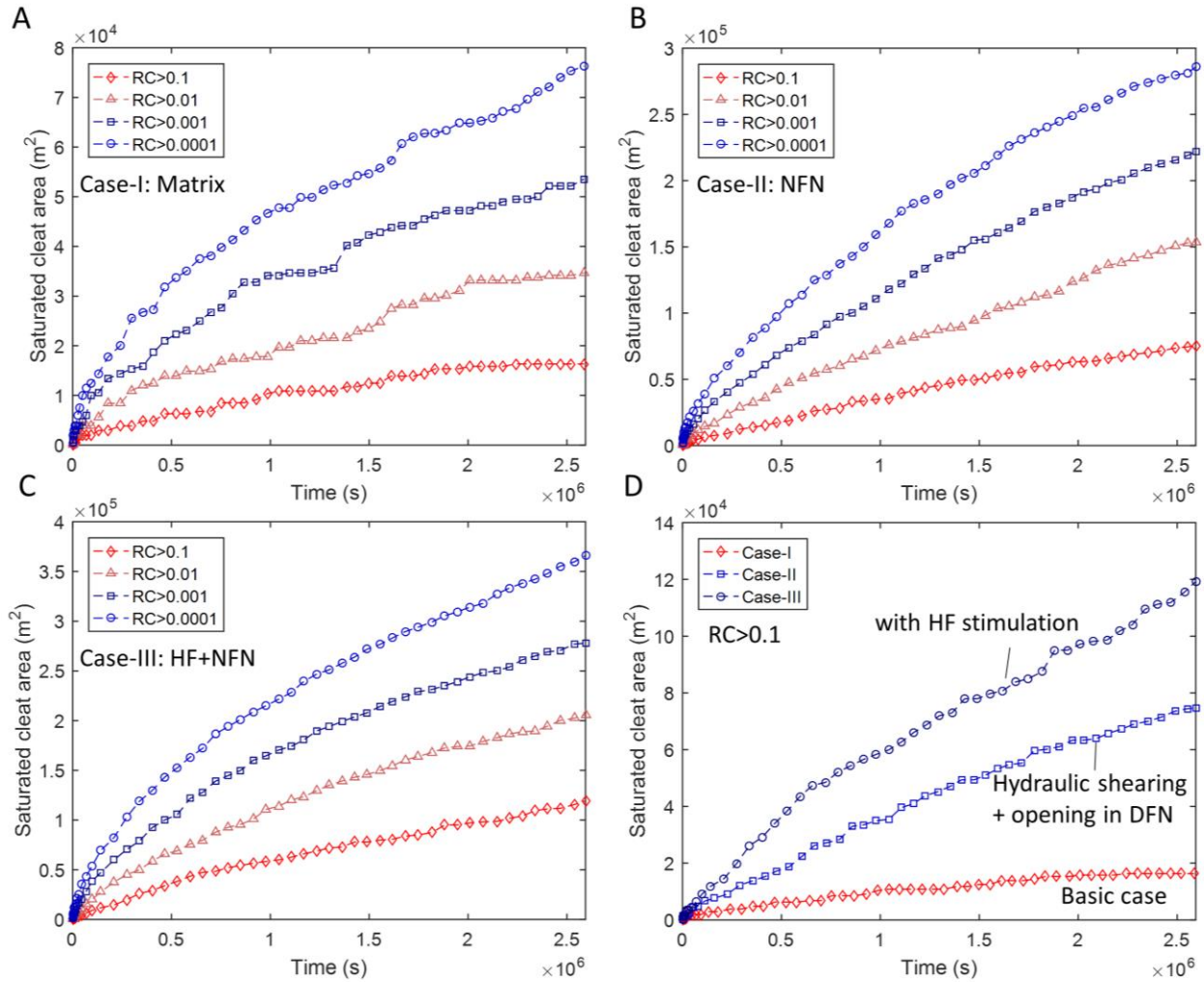


**Figure 15.** Saturated cleat area (SCA) increases with injection time in the three modeling cases. Four concentration tiers are used in the range of RC from  $>0.00001$  to  $>0.1$  at 10-fold intervals.

#### 4.4 Proppant embedment

The effect of proppant embedment in hydraulic fractures is also investigated in this simulation. Large magnitudes of proppant embedment will result in compaction and fracture diagenesis of the newly-generated hydraulic fractures and impede their conductivity. Hence, solute transport within the fracture system will be significantly influenced by the indentation of proppant into coal matrix. From Eq. (14), the higher the cohesive strength  $C$ , the more difficult to penetrate the coal matrix in compression and thus the lower the proppant embedment. Fig. 16 shows how apertures near the inlet change with the duration of injection for different cohesive strengths. Cohesive strength of the coal is set to 2.0, 2.5, and 3.0 MPa for each scenario, respectively. Even distribution of a single-layer of proppant is assumed in all cases. The initial aperture before re-injection of the nutrient solution is 0.11 mm in the case for  $C = 2$  MPa (larger proppant embedment due to weaker fracture wall), while the initial aperture before nutrient re-injection in the case of  $C = 3$  MPa is 0.24 mm (stronger fracture wall). It can be concluded that the aperture evolution curve in each case increases at first but then ceases when fluid pressures peak. Clearly, with higher cohesion  $C$ , fracture aperture increases more quickly and finally reaches a larger maximum. Fig. 17 shows the permeability distribution and pressure distribution for different cohesions,  $C$ , both before and after 30 days of injection. Before injection, the maximum initial permeability of hydraulic fractures is  $3.1 \times 10^{-16} \text{ m}^2$  and  $8.9 \times 10^{-16} \text{ m}^2$  in cases of  $C = 2$  and 3 MPa, respectively. After 30 days of injection, the maximum fracture permeability is raised to  $8.0 \times 10^{-14} \text{ m}^2$  in the case of  $C = 3$  MPa, but only to  $2.60 \times 10^{-14} \text{ m}^2$  in the case of  $C = 2$  MPa. The pressure distributions in Fig. 17 also shows that the zone of elevated pressure invades a larger area in the case of  $C = 3$  MPa. The higher and wider pressure distribution will result in a highly permeable fracture network that comprises both dilated hydraulic- and natural-fractures. It is

worth noting that some of the far-field natural fractures that are not directly connected with hydraulic fractures are also opened in the cases of a fracture wall cohesion of  $C = 3$  MPa, as shown in Figure 17. However, this does not occur in the case of  $C = 2$  MPa. The saturated cleat area after 30-days of injection for different proppant embedments are shown in Fig. 18. The saturated cleat area is approximately reduced to  $2/3$  when cohesion is decreased by 33%, due to the influence of increased proppant embedment.

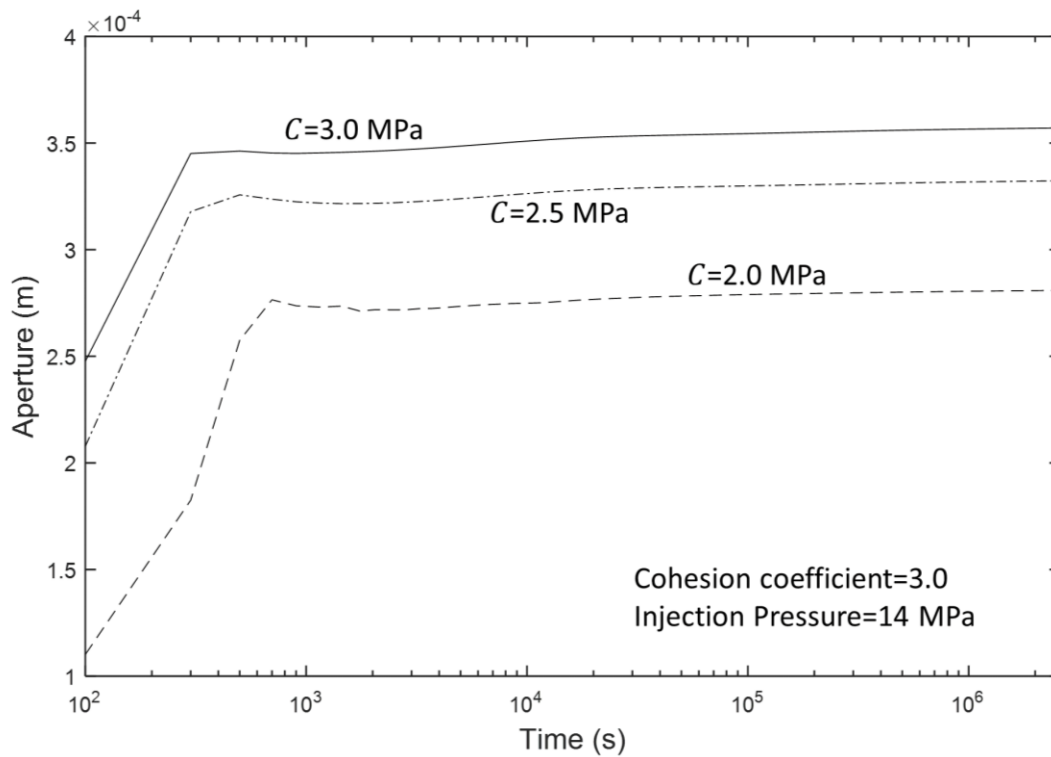


**Figure 16.** Aperture evolution near the inlet for the cases with different cohesion  $C$ .

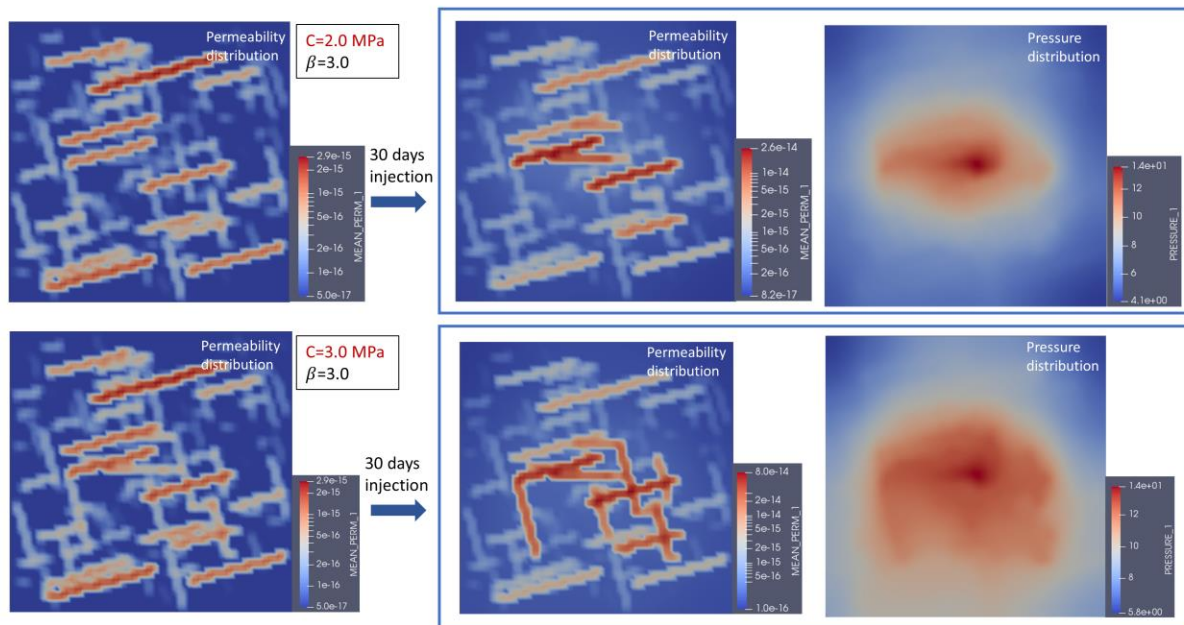


**Figure 17.** Permeability and pressure distributions before and after 30-days of injection for different cohesions.

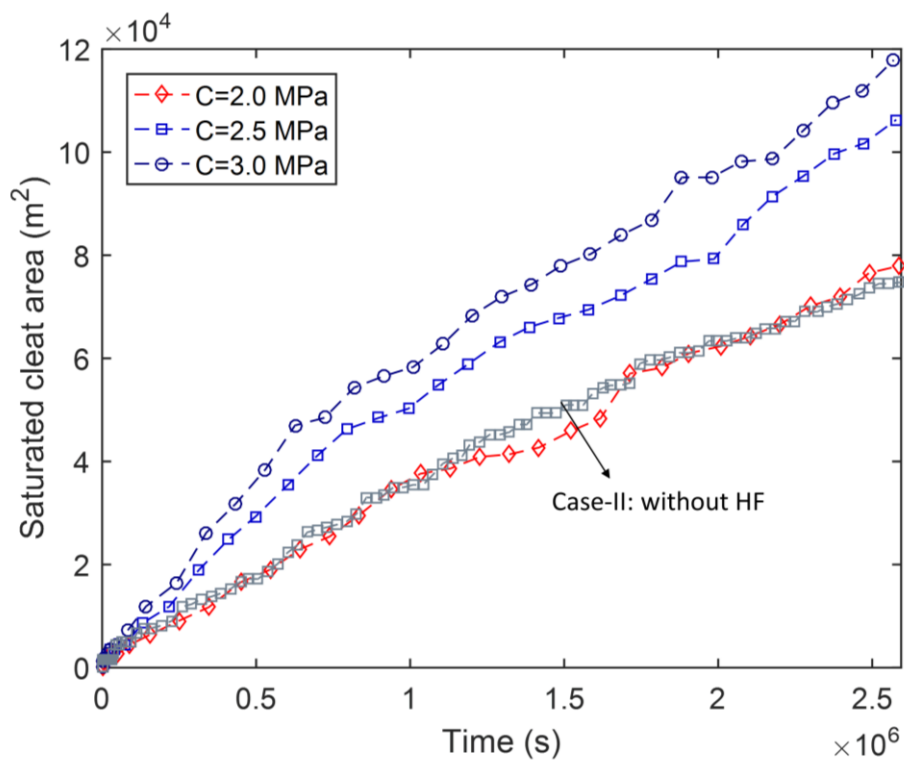


**Figure 18.** Saturated cleat areas in the cases of different cohesions (proppant embedments).

#### 4.4. Influence of Injection conditions

One potential method to enhance nutrient delivery is to increase the injection pressure and thereby the flow rate. To investigate the influence of increasing injection pressure, two more scenarios of injection at 12- and 16-MPa inlet pressure are simulated (14MPa is the default). The evolution of fracture aperture near the inlet is examined for Case-III under these different injection pressures. At the conclusion of the injection, maximum aperture near the inlet is raised from  $3.14 \times 10^{-4}$  m to  $3.59 \times 10^{-4}$  m when the pressure increases from 12 MPa to 16 MPa. Meanwhile, the permeability reaches  $7.91 \times 10^{-14}$  m<sup>2</sup> – doubling the original magnitude. Fig. 19 shows the resultant cumulative injection volume at the three injection pressures. Once the fracture closest to the inlet is dilated, an extremely permeable pathway results. The fluid pressure quickly builds in the open fracture and then penetrates the closed fractures that are connected to it. Although the fracture system has a higher permeability at high fluid pressures, flow rate will increase slowly when the fluid pressure is close to the injection pressure. At the final stage of the injection, cumulative injection will only increase at a very slow rate. In the case of 12-MPa injection, the cumulative injected nutrient volume is  $4.16 \times 10^4$  L, which is 70% of that in the case with an injection pressure of 14 MPa. Saturated surface areas ( $RC > 0.1$ ) of the cases under different injection pressures are summarized in Fig. 20. A pronounced reduction in the mineral-saturated cleat area can be seen when injection pressure decreases from 16 MPa to 10 MPa in all three cases. The results demonstrate that increasing the injection pressure is a particularly effective way to enhance nutrient delivery in MECBM.

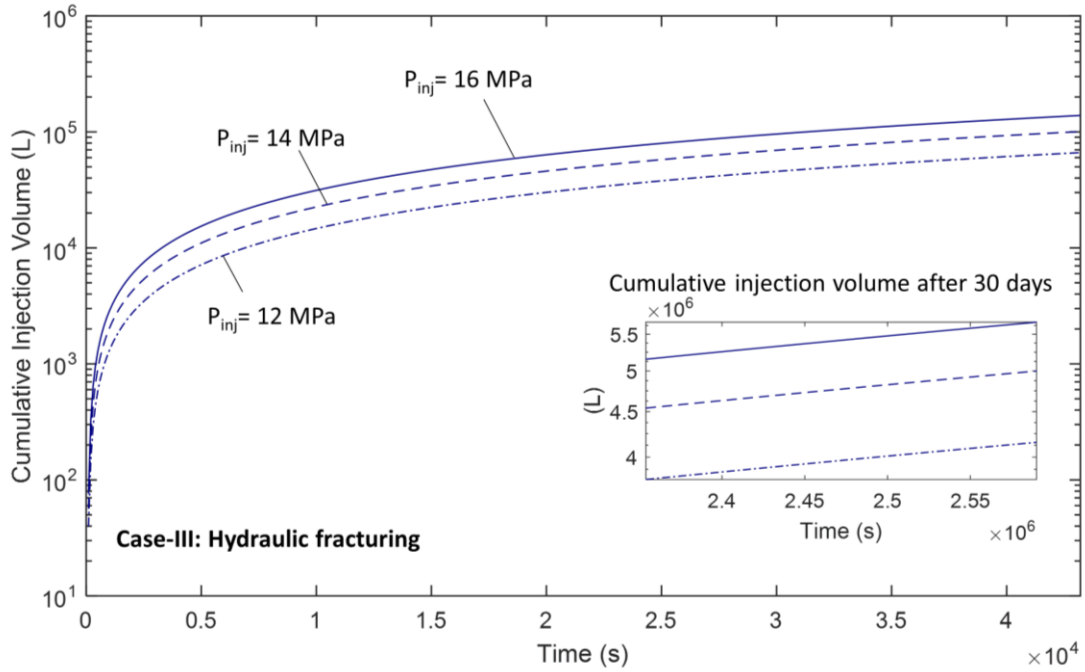


**Figure 19.** Cumulative injection volume versus time at different injection pressures.

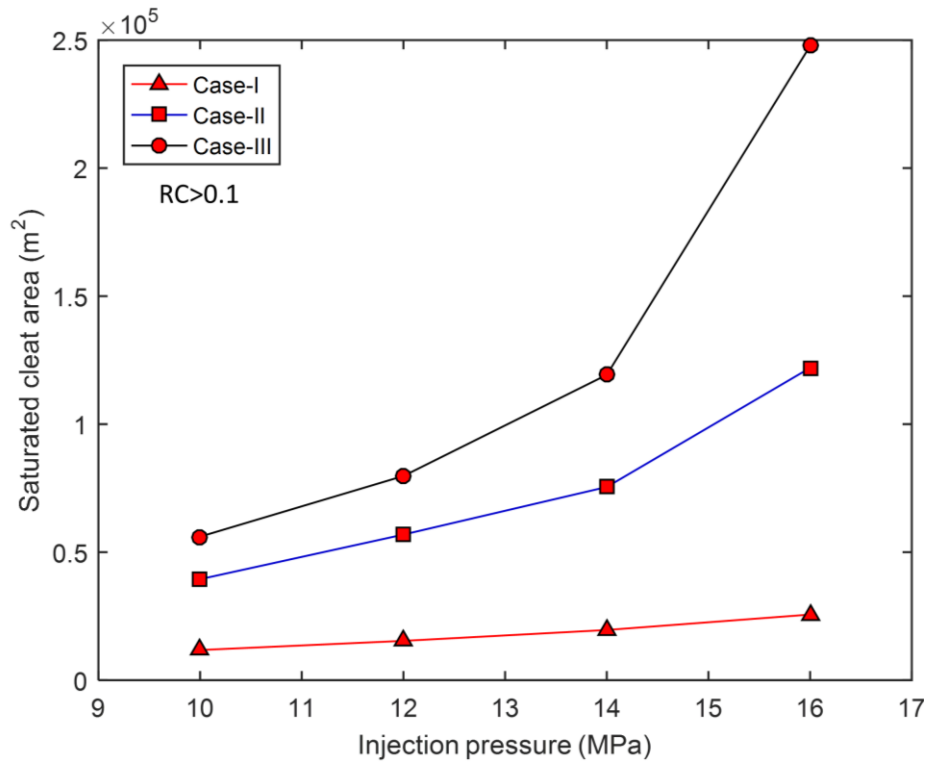


**Figure 20.** Influence of injection pressure in increasing saturated cleat area ( $RC > 0.1$ ). Note that injection pressure is set constant over the first 30 days in all 12 runs.

#### 4.5 Estimation of methane yields

From the foregoing, the microbial generation of methane may be scaled to field scale using the appropriate nutrient-penetration. Bio-gasification progresses with a time-lag while the environment become stable after injection and metabolization ultimately evolves. Once methane generation initiates, the methane yields can be estimated as a function of time as (Saurabh & Harpalani, 2018):

$$MY(t) = m \left[ \frac{KP_0}{P_0 + (K - P_0)e^{-rt}} - P_0 \right] \quad (38)$$

where  $MY(t)$  is the methane yield (mmol/g) and  $t$  is time (hours).  $m$  is a constant of proportionality (equal to unity, here).  $K$  is the carrying capacity of the environment,  $P_0$  is the initial population in the environment,  $r$  is the growth rate coefficient.

Reported rates of methane production in the laboratory bio-gasification of coal can be up to 2900 ft<sup>3</sup>/ton (4.38 mmol/g), while more moderate results show methane yields are typically in the range of 100~500 ft<sup>3</sup>/ton (0.15~0.75 mmol/g) (Bi et al., 2017; Davis et al., 2018; Green et al., 2008; Huang et al., 2013; Zhang et al., 2016a; Zhang et al., 2015; Zhang et al, 2016b). A few experiments also show an extremely low production <10 ft<sup>3</sup>/ton (0.015 mmol/g) that is not considered in this study. These production differences primarily result from the selection and characteristics of supplemented amendments, temperatures, pH values, microbial compositions, and mesh sizes and ranks of coal. Methane production rates of 120.4 ft<sup>3</sup>/ton (0.17 mmol/g) reported by Green et al. (2008) and of 464.0 ft<sup>3</sup>/ton (0.7 mmol/g) reported by Bi et al. (2017) are used in this evaluation as the baseline and optimal model, respectively. Both of these used ground coal samples at 40 mesh and the influence of the large surface area of powdered coal are

excluded in the calculations. As listed in Table 5 and plotted in Fig. 21, the numerical modeling results using the designed parameters effectively replicate experimental results.

Table 5. Modeling parameters used in the logistic equation.

	<b>Model #1 (Green et al., 2008)</b>	<b>Model #2 (Bi et al., 2018)</b>
$P_0$ (mmol/g)	0.013	0.008
K (mmol/g)	0.165	0.70
R ( $\text{hr}^{-1}$ )	0.0066	0.0059

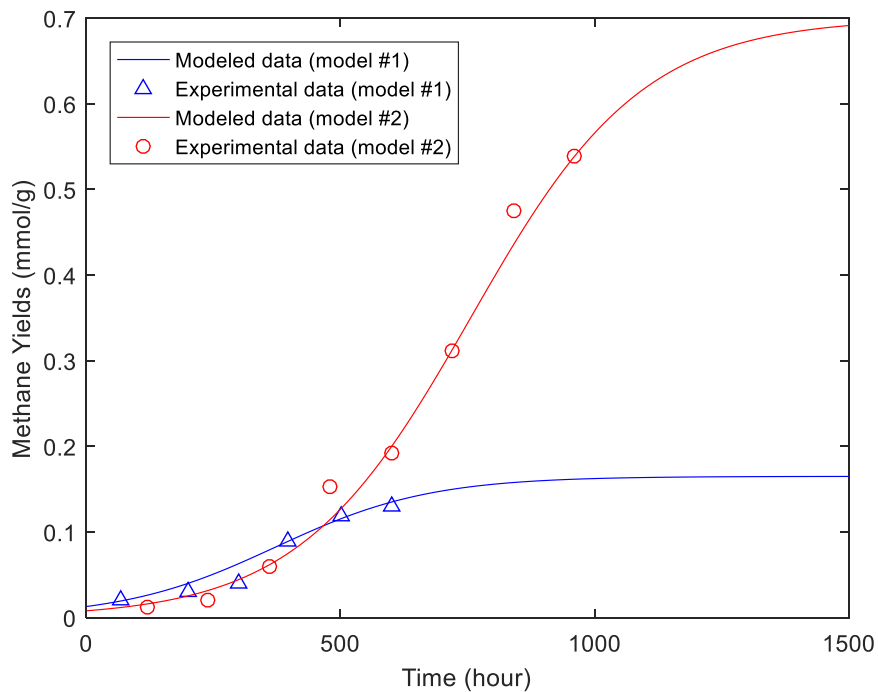


**Figure 21.** Prediction of methane yields validated by reported experimental data.

The maximum production rate is only achieved in an optimal environment with the added amendments at the optimal concentrations. However, a nutrient concentration gradient exists from the inlet to the far field following injection, as shown in the simulated results discussed

above. For a more accurate prediction of methane yield, it is important to consider the production rate at different nutrient concentrations. To quantify the influence of concentration, an empirical equation proposed by Bi et al. (2017) is adopted in this study. Finally, the prediction equation for methane yields can be expressed as

$$MY(t) = m \left[ \frac{KP_0}{P_0 + (K - P_0)e^{-rt}} - P_0 \right] \times MYR(RC) \quad (39)$$

where  $MYR(RC) = -0.5504RC^2 + 1.6954RC - 0.144$ . MYR is the methane yield ratio as a function of relative concentration of the nutrient components. To aid direct comparison, all the concentrations of primary components are normalized as relative concentrations. In this equation, the optimal values for ethanol, methanol, 2-propanol and sodium acetate are 27, 50, 10, and 100 mM, respectively.

The evolution of methane yields in Cases-I, -II and -III predicted via the two production models are shown in Fig. 22, where (A) and (B) are for the baseline model and the optimal model, respectively. The red-shaded zones represent the areas that have been largely saturated by nutrient and reach the maximum production rate after 60 days. The results identify that maximum methane production is in the range spanning 7.34 to 30.69 ft<sup>3</sup>/ton (0.011 to 0.046 mmol/g) by using different stimulation methods. The reported methane production in the Illinois and the Powder River basins are ~70 ft<sup>3</sup>/ton (Green et al., 2008; Mardon et al., 2014) – suggesting that the bio-stimulated production may reach half of its original production. Fig. 23 compares the cumulative methane yields from all scenarios. Cumulative methane yields range from  $3.73 \times 10^5$  to  $1.67 \times 10^6$  ft<sup>3</sup> in the case where nutrient transport is restricted to through the coal matrix. By using both NF network and HF stimulations, the cumulative methane yields can

be boosted 4.1-fold and 5.4-fold, respectively. In the optimal scenario (Case-III + model #2 at 16-MPa injection pressure), the biogenic methane augmented over primary recovery is  $1.22 \times 10^7$  ft<sup>3</sup>, which can be produced at a rate of 200 Mcf/d for 61 days.

All prior calculations are centered around the case study in this paper. Compared to existing evaluations of MECBM recovery noted in the literature, the influences of fracture system and coal surface area are carefully considered. This paramount importance of fracture connectivity is highlighted in the production results. It can be seen that the estimated increases in methane yields are encouraging for pre-stimulation of the reservoir. However, it is still difficult to fully evaluate MECBM due to uncertainties in in-situ microbial activity and underground hydrogeologic factors. The surface area of coal available for bio-gasification is an important variable and is ill-constrained in CBM reservoirs. These factors must be further constrained to reduce uncertainties in the prediction of microbially-enhanced methane yields.

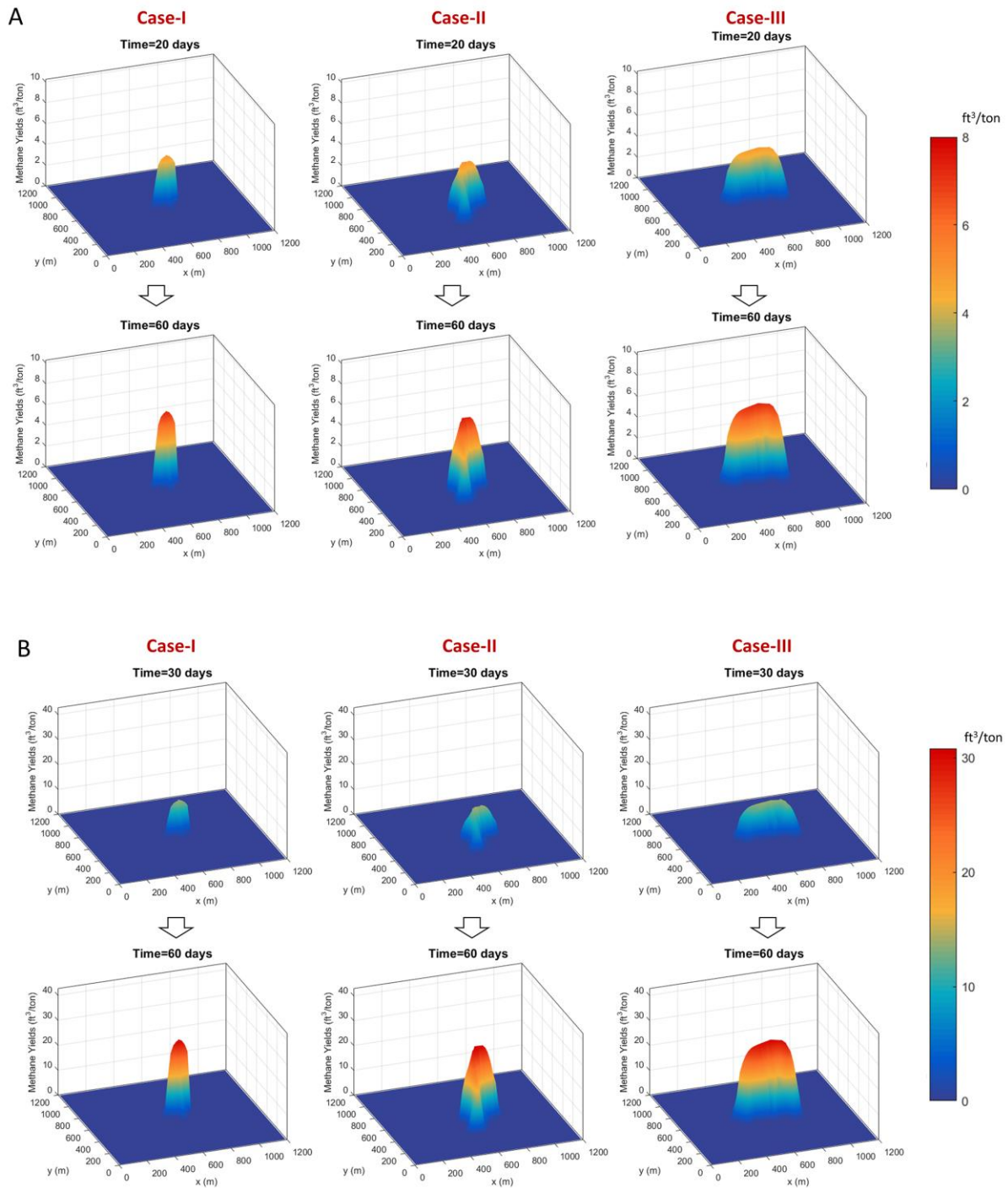


**Figure 22.** Evolution of methane yields for the three cases using (A) the baseline production model and (B) the optimal production model.

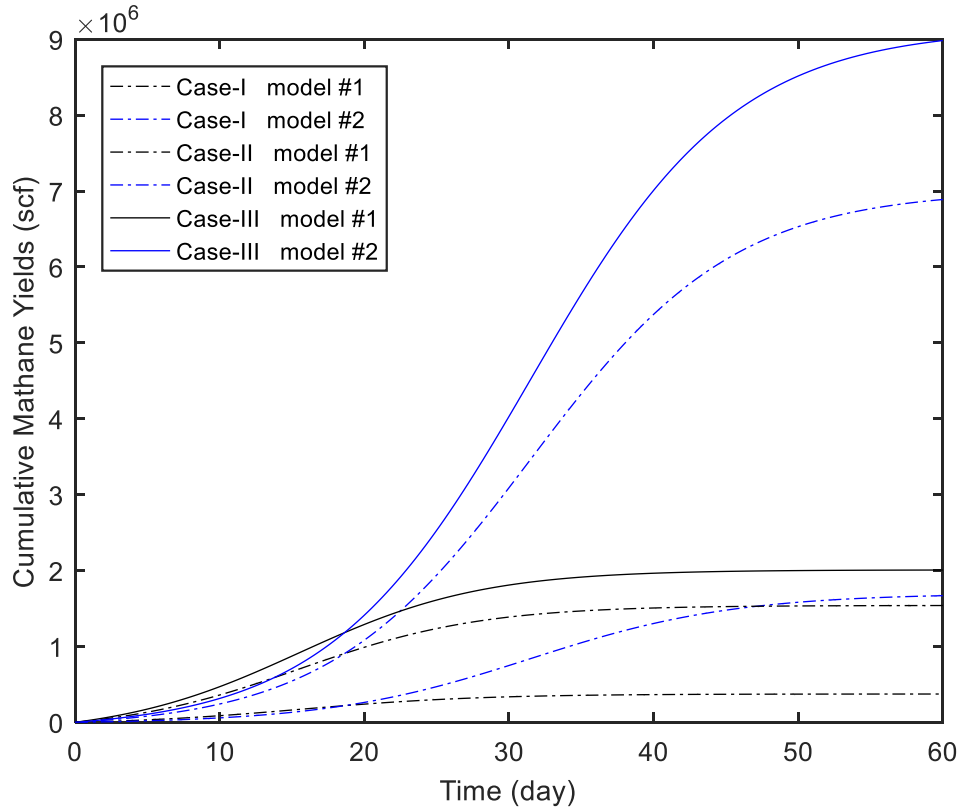


**Figure 23.** Cumulative methane yields in the three cases using the baseline production model (model #1) and the optimal production model (model #2).

## 5. Conclusions

Field-scale numerical simulations of MECBM are completed using an equivalent multi-continuum method to define the effectiveness of nutrient delivery. The complex fracture pattern of natural reservoirs is represented by an overprinted discrete fracture network (DFN) to depict natural heterogeneity and anisotropy of fracture permeability in the CBM reservoir. An aperture evolution model including fracture opening, closure and propping for both natural and hydraulically-driven fracture networks is proposed to estimate permeability evolution of the DFN. A simplified PKN model is adopted to simulate fracture propagation based on the theory of linear elastic fracture mechanics (LEFM). According to the maximum circumferential normal

stress criterion, a mixed mode I-II compression-shear failure criterion under high fluid pressure is used to generate wing fractures when hydraulic fractures interact with the pre-existing fracture network.

A prototypical MECBM reservoir is studied. Compared to the unstimulated and dilated cases of the natural fracture network, the hydraulically stimulated case demonstrates the effectiveness of hydraulic fracturing to enhance nutrient delivery. Cumulative injection volume and saturated cleat area are analyzed in each case. Concentration evolution patterns of all the media are compared. The results show that without a natural fracture system, the ability to deliver nutrient through the coal matrix is extremely limited. Pre-existing natural fractures oblique to the principal stress direction provide more permeable pathways for solute transport and nutrient delivery. Hydraulically stimulated fracture pathways, especially when connecting to a natural fracture network, may optimally deliver soluble nutrients to significant distances from the injection well, thereby increasing nutrient delivery and the efficiency of methane recovery. However, this behavior may be curtailed by the effects of proppant embedment. Decreasing proppant embedment and increasing injection pressure can facilitate the nutrient transport. In the optimal scenario, methane yields in the stimulated case is improved 5-fold that of the unstimulated case.

## Appendix A – Validation of fracture model

The coupled mechanical and fluid transport models used in this study have been rigorously validated and are reported elsewhere (Gan & Elsworth, 2016; Taron, Elsworth, & Min, 2009b). Here, the proposed fracture propagation model and the evolution of the aperture change for the propped fracture are examined.

To verify the proposed fracture propagation model we compare the simulation results against asymptotic solutions (Kovalyshen & Detournay, 2010; Nordgren, 1972). We use dimensionless variables in space and time ( $x$  and  $t$ ) and on parameters  $H$ ,  $Q_0$ ,  $E$ ,  $\mu$ , and  $C_1$  to define:

$$\tau = \frac{t}{t^*}, \quad \gamma = \frac{l}{l^*}, \quad \Omega = \frac{w}{w^*} \quad (26)$$

where  $\tau$ ,  $\gamma$ ,  $\Omega$  represent dimensionless time, length and width, respectively. The three characteristic quantities comprising fluid and rock properties are formulated as

$$t^* = \frac{\pi^2 H^6 p^{*5}}{4E^4 \mu Q_0^2}, \quad l^* = \frac{\pi H^4 p^{*4}}{4E^3 \mu Q_0}, \quad w^* = \frac{\pi H p^*}{2E}. \quad (27)$$

where  $p^* = 1$  MPa is the characteristic pressure. After identifying the scaling scheme, the small time asymptotic solution can be written as

$$\gamma(\tau) = \gamma_{m0} \tau^{4/5}, \quad \Omega(\xi, t) = \Omega_{m0}(\xi) \tau^{1/5}, \quad \tau \ll 1 \quad (28)$$

where the coordinate  $\xi = \frac{x}{l} (0 \leq \xi \leq 1)$ ,

$$\gamma_{m0} \cong 1.0006328, \quad (29)$$

$$\Omega_{\text{mo}} = \left(\frac{12}{5}\right)^{\frac{1}{3}} \gamma_{\text{m}0}^{\frac{2}{3}} (1-\xi)^{\frac{1}{3}} \left(1 - \frac{1}{96}(1-\xi)\right) + O\left((1-\xi)^{\frac{7}{3}}\right). \quad (30)$$

The large time asymptotic solution can be written as

$$\gamma(\tau) = \gamma_{\text{m}0} \tau^{1/2}, \quad \Omega(\xi, t) = \Omega_{\text{m}0}(\xi) \tau^{1/8}, \quad \tau \gg 1 \quad (31)$$

where

$$\gamma_{\text{m}0} = \frac{2}{\pi C}, \quad (32)$$

$$C = \frac{C_l H^2 p^{*2}}{\mu^{1/2} E Q_0}, \quad (33)$$

$$\Omega_{\text{m}0}(\xi) = \left(\frac{8}{\pi C}\right)^{\frac{1}{4}} \left(\frac{2}{\pi} \xi \arcsin \xi + \frac{2}{\pi} \sqrt{1-\xi^2} - \xi\right)^{1/4}. \quad (34)$$

A 1-D hydraulic fracture propagation model is simulated from  $\tau=10^{-5}$  to  $\tau=10^5$  to ensure accuracy at both small and large time scales used in this analytic approximation. The parameters used in this validation are listed in Table 1 (Wang et al., 2018). After simulation, the defined fracture length  $l$  is then transformed to  $\gamma(\tau)$  by Eqs. (26) and (27) and the comparison plotted in Fig. 4. The blue solid line shows the solved hydraulic fracture profile without connecting with any branch of a natural fracture. The red and orange solid curve shows how hydraulic fracture length evolves, with a 10m and 20m natural fracture at  $x=0.1$  m, respectively. Note that the connected natural fractures remain a constant length during injection. As apparent in Fig. 4, The numerical results fit the small and large asymptotic solution very well. The results indicate that

the connection with the natural fracture has a dominant effect on fluid leak-off at relatively small-time scale and this effect is positively correlated with the length of the connected fractures.

**Table 1.** Modeling parameters for the validation of the proposed PKN model.

Parameter	Value
Young's modulus of coal ( $E$ )	2.45 GPa
Fluid dynamic viscosity ( $\mu$ )	0.1 Pa·s
Injection rate ( $Q_o$ )	0.05 m <sup>3</sup> / s
Poisson's ratio of coal ( $\nu$ )	0.30
Height of coal seam ( $H$ )	10 m
Leak-off coefficient ( $C_l$ )	5e-5 m·s <sup>1/2</sup>

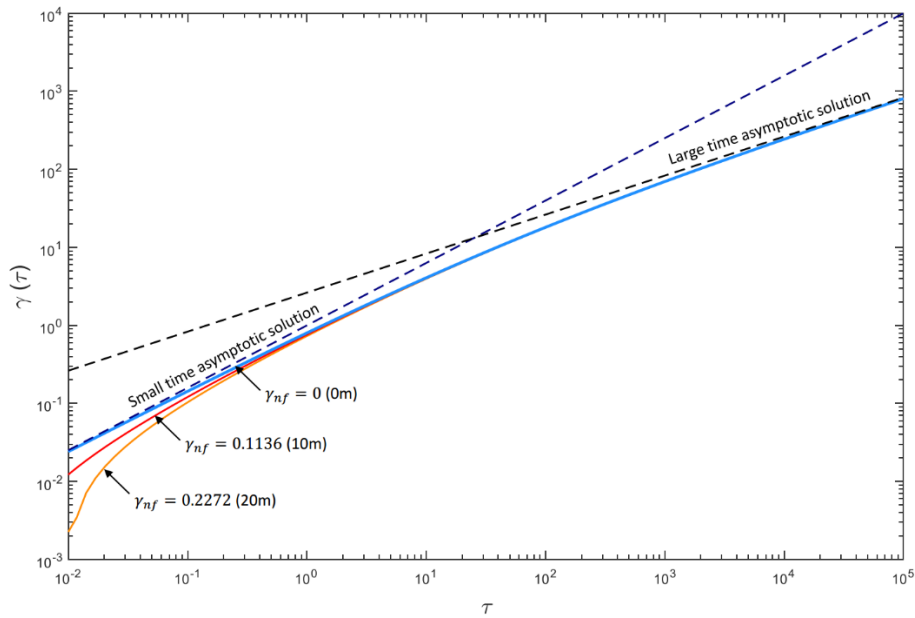


**Figure 4.** Comparison between this model and the small and large time asymptotic solutions.  $\gamma_{nf}$  represents dimensionless length of the connected natural fracture at the initiation of hydraulic fracture propagation.



## Appendix B – Validation of proppant embedment model

The mechanistic model used to describe proppant embedment and the evolution to residual aperture under normal stress is examined against experimental result and other existing models. The experimental data and modeling parameters are obtained from Lacy (1998). In this validation, the proposed model and three other theoretical models (Huitt and Mcglothlin, 1958; Li et al., 2015; Guo et al., 2017) use the parameters listed in Table 2.

**Table 2.** Modeling parameters for the validation of proppant embedment.

Parameter	Value
Young's modulus of proppant ( $E_1$ )	21.31 GPa
Young's modulus of rock ( $E_2$ )	1.17 GPa
Poisson's ratio of proppant ( $\nu_1$ )	0.144
Poisson's ratio of rock ( $\nu_2$ )	0.30
Elastic modulus reduction ratio ( $R_m$ )	0.1
Cohesive strength of rock ( $C$ )	3 MPa
Proppant size (-)	20/40

The modeled magnitudes of proppant embedment slightly underestimate the experimental data. This is presumably due to the idealized assumptions of even paving, uniform size and hard sphericity of proppants (Li et al., 2014) – conditions that are not necessarily met in practice. To optimize the prediction, two fitting parameters,  $f_\alpha$  and  $f_\beta$ , are introduced as:

$$h = f_\alpha \cdot R \left( 1 - \sqrt{1 - \frac{\sigma'}{\pi C \cdot f_\beta}} \right) + \Delta D_1 \quad (35)$$

Similar fitting parameters are also used in the three other models. The fitting parameters for each model are listed in Table 3. Fig. 5 shows the comparison between the theoretical results and the

experimental data. The proposed model is in close agreement with the experimental data within the selected range of effective stresses (0-20 MPa).

**Table 3.** Fitting parameters for the validation of proppant embedment models.

Parameters	Proposed model	Guo et al (2017)	Li et al (2014)	Huitt et al (1958)
$f_\alpha$	1.8	-	2.0	1.8
$f_\beta$	1.55	3.8	1.8	0.8 and 2.5

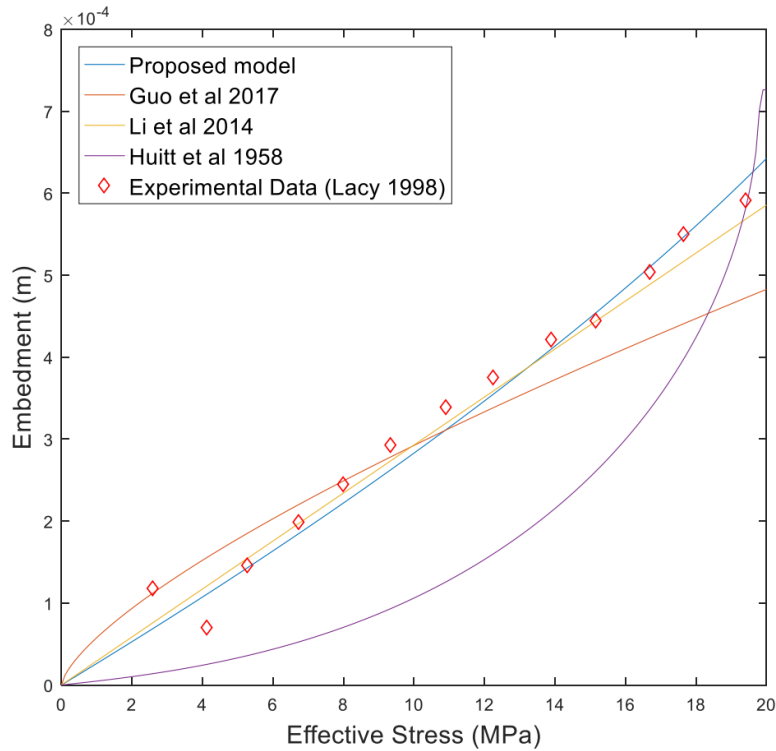


**Figure 5.** Comparison of simulation results with existing theoretical and experimental models.

### Acknowledgement

This work is a partial result of support from the Department of Energy under grant DE-FE0026161. This support is gratefully acknowledged.

## Reference

- Alramahi, B., & Sundberg, M. I. (2012). Proppant Embedment And Conductivity of Hydraulic Fractures In Shales. *International Journal of Engineering Science*, 77, 14–23. <https://doi.org/10.1016/j.ijengsci.2013.12.005>
- Bai, M., Meng, F., Elsworth, D., Abousleiman, Y., & Roegiers, J. (1999). Numerical Modelling of Coupled Flow and Deformation in Fractured Rock Specimens. *International Journal for Numerical and Analytical Methods in Geomechanics*, 23(February 1997), 141–160. [https://doi.org/10.1002/\(SICI\)1096-9853\(199902\)23:2](https://doi.org/10.1002/(SICI)1096-9853(199902)23:2)
- Bi, Z., Zhang, J., Park, S., Harpalani, S., & Liang, Y. (2017). A formation water-based nutrient recipe for potentially increasing methane release from coal in situ. *Fuel*, 209(July), 498–508. <https://doi.org/10.1016/j.fuel.2017.08.008>
- Blanton, T. (1986). Propagation of hydraulically and dynamically induced fractures in naturally fractured reservoirs. *SPE Unconventional Gas Technology Symposium*, 613–621. <https://doi.org/10.2523/15261-MS>
- Cokar, M., Ford, B., Kallos, M. S., & Gates, I. D. (2013). New gas material balance to quantify biogenic gas generation rates from shallow organic-matter-rich shales. *Fuel*, 104, 443–451. <https://doi.org/10.1016/j.fuel.2012.06.054>
- Daneshy, a A. (2003). Off-Balance Growth : A New Concept in Hydraulic Fracturing, (April), 78–85. <https://doi.org/10.2118/80992-MS>
- Davis, K. J., Lu, S., Barnhart, E. P., Parker, A. E., Fields, M. W., & Gerlach, R. (2018). Type

- and amount of organic amendments affect enhanced biogenic methane production from coal and microbial community structure. *Fuel*, 211(June 2017), 600–608. <https://doi.org/10.1016/j.fuel.2017.09.074>
- Detournay, E., Cheng, a. H.-D., & McLennan, J. D. (1990). A Poroelastic PKN Hydraulic Fracture Model Based on an Explicit Moving Mesh Algorithm. *Journal of Energy Resources Technology*, 112(4), 224. <https://doi.org/10.1115/1.2905762>
- Elsworth, B. D., & Bai, M. (1992). Flow-Deformation Response of Dual-Porosity Media, 118(1), 107–124.
- Erdogan, F., & Sih, G. C. (1963). On the crack extension in plane loading and transverse shear. *Journal Basic Engr.*, 85, 519–527.
- Faiz, M., & Hendry, P. (2006). Significance of microbial activity in Australian coal bed methane reservoirs—a review. *Bulletin of Canadian Petroleum Geology*, 54(3), 261–272. <https://doi.org/10.2113/gscpgbull.54.3.261>
- Fang, Y., Elsworth, D., & Cladouhos, T. T. (2015). Estimating In-Situ Permeability of Stimulated EGS Reservoirs Using MEQ Moment Magnitude : an Analysis of Newberry MEQ Data, c(1965), 1–10.
- Gan, Q., & Elsworth, D. (2016). A continuum model for coupled stress and fluid flow in discrete fracture networks. *Geomechanics and Geophysics for Geo-Energy and Geo-Resources*, 2(1), 43–61. <https://doi.org/10.1007/s40948-015-0020-0>
- Ghassemi, a., & Zhang, Q. (2006). Porothermoelastic Analysis of the Response of a Stationary Crack Using the Displacement Discontinuity Method. *Journal of Engineering Mechanics*,

132(1), 26–33. [https://doi.org/10.1061/\(ASCE\)0733-9399\(2006\)132:1\(26\)](https://doi.org/10.1061/(ASCE)0733-9399(2006)132:1(26))

Green, M. S., Flanagan, K. C., & Gilcrease, P. C. (2008). Characterization of a methanogenic consortium enriched from a coalbed methane well in the Powder River Basin, U.S.A. *International Journal of Coal Geology*, 76(1–2), 34–45. <https://doi.org/10.1016/j.coal.2008.05.001>

Guo, J., Wang, J., Liu, Y., Chen, Z., & Zhu, H. (2017). Analytical analysis of fracture conductivity for sparse distribution of proppant packs. *Journal of Geophysics and Engineering*, 14(3), 599–610. <https://doi.org/10.1088/1742-2140/aa6215>

Huang, S., Liu, D., Yao, Y., Gan, Q., Cai, Y., & Xu, L. (2017). Natural fractures initiation and fracture type prediction in coal reservoir under different in-situ stresses during hydraulic fracturing. *Journal of Natural Gas Science and Engineering*, 43, 69–80. <https://doi.org/10.1016/j.jngse.2017.03.022>

Huang, Z., Urynowicz, M. A., & Colberg, P. J. S. (2013). Stimulation of biogenic methane generation in coal samples following chemical treatment with potassium permanganate. *Fuel*, 111, 813–819. <https://doi.org/10.1016/j.fuel.2013.03.079>

Jamari, J., & Schipper, D. J. (2006). Experimental Investigation of Fully Plastic Contact of a Sphere Against a Hard Flat. *Journal of Tribology*, 128(2), 230. <https://doi.org/10.1115/1.2164470>

Jones, E. J. P., Voytek, M. a., Corum, M. D., & Orem, W. H. (2010). Stimulation of methane generation from nonproductive coal by addition of nutrients or a microbial consortium. *Applied and Environmental Microbiology*, 76(21), 7013–7022. <https://doi.org/10.1128/AEM.00728-10>

- Ki-Bok, M., Rutqvist, J., Tsang, C. F., & Jing, L. (2004). Stress-dependent permeability of fractured rock masses: A numerical study. *International Journal of Rock Mechanics and Mining Sciences*, *41*(7), 1191–1210. <https://doi.org/10.1016/j.ijrmms.2004.05.005>
- Kirk, M. F., Martini, A. M., Brecker, D. O., Colman, D. R., Takacs-Vesbach, C., & Petsch, S. T. (2012). Impact of commercial natural gas production on geochemistry and microbiology in a shale-gas reservoir. *Chemical Geology*, *332–333*, 15–25. <https://doi.org/10.1016/j.chemgeo.2012.08.032>
- Kovalyshen, Y., & Detournay, E. (2010). A reexamination of the classical PKN model of hydraulic fracture. *Transport in Porous Media*, *81*(2), 317–339. <https://doi.org/10.1007/s11242-009-9403-4>
- Kumar, H., Elsworth, D., Liu, J., Pone, D., & Mathews, J. P. (2015). Permeability evolution of propped artificial fractures in coal on injection of CO<sub>2</sub>. *Journal of Petroleum Science and Engineering*, *133*, 695–704. <https://doi.org/10.1016/j.petrol.2015.07.008>
- Lacy, L. L., Rickards, A. R., & Bilden, D. M. (1998). Fracture Width and Embedment Testing in Soft Reservoir Sandstone. *SPE Drilling & Completion*, *13*(1), 25–29. <https://doi.org/10.2118/36421-PA>
- Lee, D. S., Elsworth, D., Yasuhara, H., Weaver, J. D., & Rickman, R. (2010). Experiment and modeling to evaluate the effects of proppant-pack diagenesis on fracture treatments. *Journal of Petroleum Science and Engineering*, *74*(1–2), 67–76. <https://doi.org/10.1016/j.petrol.2010.08.007>
- Li, K., Gao, Y., Lyu, Y., & Wang, M. (2015). New Mathematical Models for Calculating Proppant Embedment and Fracture Conductivity. *SPE Journal*, *20*(3), 496–507.

<https://doi.org/10.2118/155954-PA>

Liu, C., Zachara, J. M., Qafoku, N. P., & Wang, Z. (2008). Scale-dependent desorption of uranium from contaminated subsurface sediments. *Water Resources Research*, *44*(8), 1–13.

<https://doi.org/10.1029/2007WR006478>

Liu, J., Chen, Z., Elsworth, D., Miao, X., & Mao, X. (2011). Evolution of coal permeability from stress-controlled to displacement-controlled swelling conditions. *Fuel*, *90*(10), 2987–2997.

<https://doi.org/10.1016/j.fuel.2011.04.032>

Liu, T., Cao, P., & Lin, H. (2014). Damage and fracture evolution of hydraulic fracturing in compression-shear rock cracks. *Theoretical and Applied Fracture Mechanics*, *74*(1), 55–63.

<https://doi.org/10.1016/j.tafmec.2014.06.013>

Liu, Z., Chen, M., & Zhang, G. (2014). Analysis of the influence of a natural fracture network on hydraulic fracture propagation in carbonate formations. *Rock Mechanics and Rock Engineering*, *47*(2), 575–587.

<https://doi.org/10.1007/s00603-013-0414-7>

Lloyd, K. (2015). Beyond known methanogens. *Science*, *350*(6259), 384.

<https://doi.org/10.1126/science.aad4066>

Long, J. C. S., & Witherspoon, P. a. (1985). The relationship of the degree of interconnection to permeability in fracture networks. *Journal of Geophysical Research*, *90*(B4), 3087.

<https://doi.org/10.1029/JB090iB04p03087>

Mardon, S. M., Eble, C. F., Hower, J. C., Takacs, K., Mastalerz, M., & Marc Bustin, R. (2014). Organic petrology, geochemistry, gas content and gas composition of Middle Pennsylvanian age coal beds in the Eastern Interior (Illinois) Basin: Implications for CBM development

- and carbon sequestration. *International Journal of Coal Geology*, 127, 56–74.  
<https://doi.org/10.1016/j.coal.2014.02.002>
- McGuire, T. P., Elsworth, D., & Karcz, Z. (2013). Experimental Measurements of Stress and Chemical Controls on the Evolution of Fracture Permeability. *Transport in Porous Media*, 98(1), 15–34. <https://doi.org/10.1007/s11242-013-0123-4>
- Moore, T. A. (2012). Coalbed methane: A review. *Int. J. Coal Geol.*, 101, 36–81.  
<https://doi.org/10.1016/j.coal.2012.05.011>
- Noiriel, C., Renard, F., Doan, M. L., & Gratier, J. P. (2010). Intense fracturing and fracture sealing induced by mineral growth in porous rocks. *Chemical Geology*, 269(3–4), 197–209.  
<https://doi.org/10.1016/j.chemgeo.2009.09.018>
- Nordgren, R. P. (1972). Propagation of a Vertical Hydraulic Fracture. *Society of Petroleum Engineers Journal*, 12(4), 306–314. <https://doi.org/10.2118/3009-PA>
- Oda, M. (1986). An equivalent continuum model for coupled stress and fluid flow analysis in jointed rock masses. *Water Resources Research*, 22(13), 1845–1856.  
<https://doi.org/10.1029/WR022i013p01845>
- Olson, J. E. (2003). Sublinear scaling of fracture aperture versus length: An exception or the rule? *Journal of Geophysical Research: Solid Earth*, 108(B9).  
<https://doi.org/10.1029/2001JB000419>
- Palmer, I. (2010). Coalbed methane completions: A world view. *International Journal of Coal Geology*, 82(3–4), 184–195. <https://doi.org/10.1016/j.coal.2009.12.010>
- Park, S. Y., & Liang, Y. (2016). Biogenic methane production from coal: A review on recent

- research and development on microbially enhanced coalbed methane (MECBM). *Fuel*, *166*, 258–267. <https://doi.org/10.1016/j.fuel.2015.10.121>
- Rahman, M. M., & Rahman, M. K. (2010). A Review of Hydraulic Fracture Models and Development of an Improved Pseudo-3D Model for Stimulating Tight Oil/Gas Sand. *Energy Sources, Part A: Recovery, Utilization, and Environmental Effects*, *32*(15), 1416–1436. <https://doi.org/10.1080/15567030903060523>
- Ritter, D., Vinson, D., Barnhart, E., Akob, D. M., Fields, M. W., Cunningham, A. B., ... McIntosh, J. C. (2015). Enhanced microbial coalbed methane generation: A review of research, commercial activity, and remaining challenges. *International Journal of Coal Geology*, *146*, 28–41. <https://doi.org/10.1016/j.coal.2015.04.013>
- Rutqvist, J., Leung, C., Hoch, A., Wang, Y., & Wang, Z. (2013). Journal of Rock Mechanics and Geotechnical Engineering Linked multicontinuum and crack tensor approach for modeling of coupled geomechanics , fluid flow and transport in fractured rock. *Integrative Medicine Research*, *5*(1), 18–31. <https://doi.org/10.1016/j.jrmge.2012.08.001>
- Rutqvist, J., & Stephansson, O. (2003). The role of hydromechanical coupling in fractured rock engineering. *Hydrogeology Journal*, *11*(1), 7–40. <https://doi.org/10.1007/s10040-002-0241-5>
- Sammis, C. G., & Ashby, M. F. (1986). The failure of brittle porous solids under compressive stress states. *Acta Metallurgica*, *34*(3), 511–526. [https://doi.org/10.1016/0001-6160\(86\)90087-8](https://doi.org/10.1016/0001-6160(86)90087-8)
- Saurabh, S., & Harpalani, S. (2018). Modeling of microbial methane generation from coal and assessment of its impact on flow behavior. *Fuel*, *216*(November 2017), 274–283.

<https://doi.org/10.1016/j.fuel.2017.12.015>

Scott, A. (1999). Improving coal gas recovery with microbially enhanced coalbed methane. *Coalbed Methane: Scientific, Environmental and ...*, 89–110. [https://doi.org/10.1007/978-94-017-1062-6\\_7](https://doi.org/10.1007/978-94-017-1062-6_7)

Stephen, S., & David, M.-T. (2004). Investigating How Proppant Packs Change Under Stress. *Proceedings of SPE Annual Technical Conference and Exhibition*. <https://doi.org/10.2523/90562-MS>

Stolper, D. A., Lawson, M., Davis, C. L., Ferreira, A. A., Santos Neto, E. V., Ellis, G. S., ... Eiler, J. M. (2014). Formation temperatures of thermogenic and biogenic methane. *Science*, 344(6191), 1500–1503. <https://doi.org/10.1126/science.1254509>

Taron, J., & Elsworth, D. (2010). Coupled mechanical and chemical processes in engineered geothermal reservoirs with dynamic permeability. *International Journal of Rock Mechanics and Mining Sciences*, 47(8), 1339–1348. <https://doi.org/10.1016/j.ijrmms.2010.08.021>

Taron, J., Elsworth, D., & Min, K. B. (2009a). Numerical simulation of thermal-hydrologic-mechanical-chemical processes in deformable, fractured porous media. *International Journal of Rock Mechanics and Mining Sciences*, 46(5), 842–854. <https://doi.org/10.1016/j.ijrmms.2009.01.008>

Taron, J., Elsworth, D., & Min, K. B. (2009b). Numerical simulation of thermal-hydrologic-mechanical-chemical processes in deformable, fractured porous media. *International Journal of Rock Mechanics and Mining Sciences*, 46(5), 842–854. <https://doi.org/10.1016/j.ijrmms.2009.01.008>

- Ulrich, G., & Bower, S. (2008). Active methanogenesis and acetate utilization in Powder River Basin coals, United States. *International Journal of Coal Geology*, 76(1–2), 25–33. <https://doi.org/10.1016/j.coal.2008.03.006>
- Verne, J. (2009). Global Possibilities of Future Methane and Hydrogen Economies. *Energy*, (June), 34–39.
- Volk, L., Raible, C., Carroll, H., & Spears, J. (1981). Embedment of High Strength Proppant Into Low-Permeability Reservoir Rock. *Proceedings of SPE/DOE Low Permeability Gas Reservoirs Symposium*. <https://doi.org/10.2118/9867-MS>
- Wang, J., Elsworth, D., & Denison, M. K. (2018). Hydraulic fracturing with leakoff in a pressure-sensitive dual porosity medium. *International Journal of Rock Mechanics and Mining Sciences*, 107(April), 55–68. <https://doi.org/10.1016/j.ijrmms.2018.04.042>
- Wang, S., Elsworth, D., & Liu, J. (2012). A mechanistic model for permeability evolution in fractured sorbing media. *Journal of Geophysical Research: Solid Earth*, 117(September 2011), 1–17. <https://doi.org/10.1029/2011JB008855>
- Wang, S., Elsworth, D., & Liu, J. (2013). Permeability evolution during progressive deformation of intact coal and implications for instability in underground coal seams. *International Journal of Rock Mechanics and Mining Sciences*, 58, 34–45. <https://doi.org/10.1016/j.ijrmms.2012.09.005>
- Warren, J. E., & Root, P. J. (1963). The Behavior of Naturally Fractured Reservoirs. *Society of Petroleum Engineers Journal*, 3(3), 245–255. <https://doi.org/10.2118/426-PA>
- Wen, Q., Zhang, S., Wang, L., Liu, Y., & Li, X. (2007). The effect of proppant embedment upon

- the long-term conductivity of fractures. *Journal of Petroleum Science and Engineering*, 55(3–4), 221–227. <https://doi.org/10.1016/j.petrol.2006.08.010>
- Wu, Y., Liu, J., Chen, Z., Elsworth, D., & Pone, D. (2011). A dual poroelastic model for CO<sub>2</sub>-enhanced coalbed methane recovery. *International Journal of Coal Geology*, 86, 177–189. <https://doi.org/10.1016/j.coal.2011.01.004>
- Zhang, J., Kamenov, A., Zhu, D., & Hill, D. (2013). Laboratory Measurement of Hydraulic Fracture Conductivities in the Barnett Shale. *International Petroleum Technology Conference*, 1–12. <https://doi.org/10.2523/16444-MS>
- Zhang, J., Liang, Y., & Harpalani, S. (2016). Optimization of methane production from bituminous coal through biogasification. *Applied Energy*, 183, 31–42. <https://doi.org/10.1016/j.apenergy.2016.08.153>
- Zhang, J., Liang, Y., Pandey, R., & Harpalani, S. (2015). Characterizing microbial communities dedicated for conversion of coal to methane in situ and ex situ. *International Journal of Coal Geology*, 146, 145–154. <https://doi.org/10.1016/j.coal.2015.05.001>
- Zhang, J., Park, S. Y., Liang, Y., & Harpalani, S. (2016). Finding cost-effective nutrient solutions and evaluating environmental conditions for biogasifying bituminous coal to methane ex situ. *Applied Energy*, 165, 559–568. <https://doi.org/10.1016/j.apenergy.2015.12.067>
- Zhang, X., & Jeffrey, R. G. (2014). Role of overpressurized fluid and fluid-driven fractures in forming fracture networks. *Journal of Geochemical Exploration*, 144(PA), 194–207. <https://doi.org/10.1016/j.gexplo.2014.03.021>

Zhao, Z., Jing, L., & Neretnieks, I. (2010). Evaluation of hydrodynamic dispersion parameters in fractured rocks. *Journal of Rock Mechanics and Geotechnical Engineering*, 2(3), 243–254.

<https://doi.org/10.3724/SP.J.1235.2010.00243>

Zou, M., Wei, C., Zhang, M., Shen, J., Chen, Y., & Qi, Y. (2013). Classifying coal pores and estimating reservoir parameters by nuclear magnetic resonance and mercury intrusion porosimetry. *Energy and Fuels*, 27(7), 3699–3708. <https://doi.org/10.1021/ef400421u>